Contents lists available at ScienceDirect

Comput. Methods Appl. Mech. Engrg.
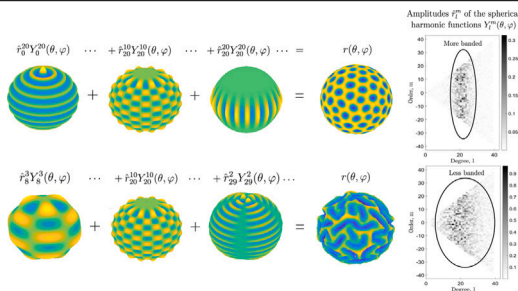
journal homepage: www.elsevier.com/locate/cma

Spherical harmonics-based pseudo-spectral method for quantitative analysis of symmetry breaking in wrinkling of shells with soft cores

Jan Zavodnik[1], Miha Brojan[*]

Faculty of Mechanical Engineering, University of Ljubljana, 1000 Ljubljana, Slovenia

GRAPHICAL ABSTRACT

ARTICLE INFO

ABSTRACT

A complete understanding of the wrinkling of compressed films on curved substrates remains illusive due to the limitations of both analytical and current numerical methods. The difficulties arise from the fact that the energetically minimal distribution of deformation localizations is primarily influenced by the inherent nonlinearities and that the deformation patterns on curved surfaces are additionally constrained by the topology. The combination of two factors – the need for dense meshes to mitigate the topological limitations of discretization in domains such as spheres where there is no spherically-symmetric discretizations, and the intensive search for minima in a highly non-convex energy landscape due to nonlinearity – makes existing numerical methods computationally impractical without oversimplifying assumptions to reduce computational costs or introducing artificial parameters to ensure numerical stability. To solve these issues, we have developed a novel (less) reduced version of shell theory for shells subjected to membrane loads, such as during wrinkling. It incorporates the linear contributions of the usually excluded tangential displacements in the membrane strain energy and thus retains the computational efficiency of reduced state-of-the-art methods while nearly achieving the accuracy of the full Kirchhoff–Love shell theory.

We introduce a Galerkin-type pseudo-spectral method to further reduce computational costs, prevent non-physical deformation distribution due to mesh-induced nucleation points, and avoid singularities at the poles of the sphere. The method uses spherical harmonic functions

---

* Corresponding author.
  E-mail address: miha.brojan@fs.uni-lj.si (M. Brojan).
[1] Present address: SISSA–International School for Advanced Studies, 34136 Trieste, Italy.

to represent functions on the surface of a sphere and is integrated into the framework of minimizing the total potential energy subject to constraints. This robust approach effectively solves the resulting non-convex potential energy problem. Our method accurately predicts the transition between deformation modes based solely on the material and geometric parameters determined in our experiments, without the need to introduce artificial parameters for numerical stability and/or additional fitting of the experimental data.

1. Introduction

In a compressed film on a compliant substrate, a significant part of the membrane strain energy is released through a symmetry breaking phenomenon, when an initially smooth surface wrinkles. This release of membrane strain energy is offset by a smaller increase in strain energy due to the bending of the film and the straining of the substrate. The bending of the film imposes a penalty on wrinkles with small wavelengths, while the strain in the substrate imposes a penalty on wrinkles with large wavelengths. As a compromise, the average wavelength of the wrinkles is somewhere in-between, so that it minimizes the total additional strain energy.

The average wrinkle wavelength is primarily influenced by the linear mechanical effects, even within moderately large deformations. On the other hand, the distribution of wrinkles is mainly determined by the nonlinear mechanical effects and their interplay with the initial curvature, and surface topology [1–3]. This complex dependency poses great challenges to the analysis of wrinkling for the following reasons: (*i*) Lack of analytical predictions: Apart from determining the average wrinkle wavelength, other analyses are hardly feasible analytically due to the dominance of nonlinear effects. This leads to a lack of fundamental understanding and hinders the development of efficient numerical methods capable of predicting the experimentally observed energy-minimizing deformation patterns. (*ii*) Complexity of bifurcation: Even with a gradual increase in load, the interaction of the initial curvature and nonlinear effects leads to a sharp transition from the unwrinkled to the wrinkled state, associated with super- or sub-critical pitchfork bifurcation. This bifurcation branches into numerous equilibrium paths with different degrees of stability. Numerical algorithms often struggle with such sharp transitions and are prone to divergence. Even if convergence is achieved, the stability or energy minimization of the solution is not guaranteed. (*iii*) Proliferation of equilibrium paths: Beyond the bifurcation point, the number of equilibrium paths with different stability and potential energy can be extremely large. Advanced state-of-the-art numerical algorithms have difficulty finding any equilibrium path, let alone the energy-minimizing one, because the stability and potential energy of these paths change as they progress. Path-following techniques, generally unaware of neighboring paths, are unable to select the energy-minimizing paths unless the number of paths is small enough and branch-switching algorithms are carefully implemented. In addition, the problem can become even more difficult when viscoelasticity is present. Although physical or artificial viscoelasticity in algorithms usually regularizes the problem and increases numerical stability, it can also introduce additional meta-stable equilibrium states, which are unreachable by purely elastic systems, and can further hinder the numerical algorithms, see [4,5].

In planar wrinkling films, some of the aforementioned problems are mitigated by the lack of initial curvature. First, there is no interaction between the curvature induced by wrinkling and the initial curvature. Second, the topology imposes no additional symmetry-breaking constraints and allows hexagonal or zigzag deformation patterns [6]. Consequently, the bifurcation is typically supercritical, leading to fewer equilibrium paths [3]. This allows some state-of-the-art commercial numerical algorithms to find solutions, although multiple trials are often required.

Conversely, both commercial and modern customized algorithms often fail in solving wrinkling on shells with non-zero Gaussian curvature. The interplay between the initial curvature and the nonlinearities usually leads to a subcritical bifurcation, which causes a discontinuous dynamic jump from a wrinkle-free to a moderately deformed state with numerous possible equilibrium solutions, see e.g. [7–9]. Furthermore, on curved surfaces, e.g. on spheres, symmetrical patterns such as hexagonal, zigzag or parallel deformations are not feasible due to topological constraints. This leads to further symmetry-breaking due to the asymmetrical arrangement of wrinkles. The problem of wrinkle arrangement on a curved surface is analogous to the Thomson problem of finding an energy-minimizing distribution of repulsive charges on a curved manifold, see [1,10–12]. As the number of wrinkles increases, the space of possible arrangements grows exponentially [13,14], which further limits the success in solving this problem, especially when using commercial numerical software. In highly symmetric systems, the distribution of deformation is poorly regulated unless there are boundary effects or initial imperfections that serve as nucleation points for wrinkle formation. In the absence of prescribed boundary effects or initial imperfections, spatial discretization of the problem can introduce non-physical deformation patterns that overshadow the mild effects of nonlinearities. In such cases, the arrangement of wrinkles is often governed by the numerical mesh that acts as the source of the initial imperfections, unless it is extremely dense (e.g. one magnitude smaller than the smallest element of the deformation pattern). Unfortunately, for thin films with a large number of wrinkles, the degrees of freedom rapidly increase. Combined with the high number of iterations required for convergence, the use of sufficiently dense meshes becomes computationally impractical. Numerous examples can be found in the literature where because a dense-enough meshes were infeasible, a strong influence is seen on the final deformation distribution, especially for systems with a medium-to-large number of wrinkles, see e.g. [7,8,15].

Due to the aforementioned challenges, current state-of-the-art computational algorithms, used with currently available computers, offer an insufficient support for understanding wrinkling on curved substrates. Consequently, even for basic geometric objects

such as cylinders, spheres and tori, the initial arrangement of dimples and their evolution into valleys and labyrinth-like patterns remains poorly understood. Despite these difficulties, some attempts have been made to study wrinkling on curved substrates using both commercial and custom-made computational algorithms. For instance, commercial finite element methods were used in studies [15–17]. However, these solutions were limited to specific cases and details of the element types and parameters used were often not provided. To overcome the computational challenges, some researchers have developed customized tools that simulate a wider range of parameters and typically use kinematic assumptions for thin shells to reduce the number of degrees of freedom. Wrinkling on cylinders and tori was investigated in studies e.g. by Lavrenčič et al. [18] and Wang et al. [19], respectively. In a study by Velding et al. [9], a special shell element was developed to analyze wrinkling without additional initial imperfections or perturbation forces. In the studies of Veldin et al. [7,8], bending contributions were linearized, tangential displacements were neglected and the substrate was modeled using Winkler-type assumptions to further reduce the number of degrees of freedom. Unfortunately, the path-following technique used was limited and rarely found the correct energy-minimizing deformation patterns. Although the deformation patterns obtained were similar to the experimental observations, the arrangement of the dimples differed slightly and the formulations failed to predict experimentally measured bifurcation loads by up to an order of magnitude. In the work by Stoop et al. [2], which inspired a series of the aforementioned studies by Veldin et al. the formulation of the wrinkling problem under certain assumptions (e.g. bending terms were linearized, tangential displacements were neglected and Winkler-type assumptions were used to model the effect of the substrate) showed an analogy to the Swift-Hohenberg partial differential equation (PDE) for thermal convection, which produces patterns similar to those observed in wrinkling. The PDE was solved using Cirak-type shell finite elements [20], with which the numerical problems associated with spatial discretization can be circumvented to some extent, although they are cumbersome to implement. Instead of the commonly used predictor–corrector iterative solution algorithm, an overdamped explicit pseudo-dynamic relaxation method was used. This method is prone to divergence in ill-posed problems and can also settle in suboptimal solutions, as shown in [4]. To regularize the originally ill-posed problem, Stoop et al. introduced an artificial correction parameter c_1 into the PDE that controls the magnitude of the nonlinear contribution of the Winkler-type substrate. This parameter was adjusted to bring the obtained deformation patterns qualitatively more in line with the experimental observations.

The correction parameter c_1 is considered necessary mainly because the Winkler-type substrate model is used and tangential displacements in the film are neglected in the theory. As demonstrated in the subsequent studies [3,8], the neglect of tangential displacements leads to fundamentally different results, resulting in discrepancies between numerical and experimental observations. In experiments, the transition to labyrinth patterns is gradual: with increasing load, pairs of dimples merge into short valleys, which further elongate and merge with neighboring valleys to eventually form a labyrinth pattern. In contrast, reduced theories that neglect tangential displacements produce only round dimples, labyrinths or mixed labyrinth-dimple patterns consisting of continuous long valleys accompanied by round dimples.

In this paper, we present a new version of the shell model to circumvent the numerical difficulties and to enable a reliable, computationally efficient quantitative analysis of wrinkling in compressed shells on soft cores. This theory does not neglect tangential displacements and membrane equilibrium, which ensures an accurate consideration of the release of membrane strain energy through both out-of-plane and tangential displacements. To increase calculation speed and robustness, the less influential bending and substrate terms are linearized. Furthermore, we use exact solutions for the mechanical response of a deformed linear elastic solid instead of relying on a heuristic approximation of the Winkler-type substrate response or increasing the computational cost by simulating the substrate response directly. This approach allows for a more accurate simulation of the behavior of the substrate while maintaining computational efficiency.

To solve the system of nonlinear PDEs on the surface of a spherical manifold, we use a spectral method with spherical harmonic functions as basis functions. This approach offers several advantages:

1. Elimination of the bias associated with the inability to discretize a topological object with a mesh that preserves the intrinsic symmetry: The spectral method translates the problem from the physical (spatial) domain, which might not be able to be discretized symmetrically, into an already discrete function space. This way (non-physical) mesh-induced nucleation points for wrinkle formation are avoided.
2. Excellent convergence properties: Spectral methods have superior convergence properties for smooth problems [21,22], which means that a minimal number of degrees of freedom are needed for an accurate solution.
3. Avoidance of singularities at the poles: In contrast to other approximation functions, spherical harmonic functions do not generate singularities at the poles, as they are eigenfunctions of the spherical coordinate system.
4. Analytical expression of operators: The use of spherical harmonic approximations makes it possible to express differential and nonlinear operators on the functions analytically as algebraic expressions without numerical errors. This transforms the problem from solving a system of differential equations in physical space to solving a system of algebraic equations in a discrete space of amplitudes of spherical harmonic functions.
5. Exact substrate response: The analytical solution of the substrate response, given in terms of the amplitudes of spherical harmonic functions, can be readily used for the calculation. This provides the precision of continuum small strain theory with the simplicity of a Winkler-type substrate model, minimizing the number of degrees of freedom. It is important to note that more complex models with nonlinear and anisotropic material behavior for the substrate can also be employed, but at a cost of some additional computational expense.
6. Determining the degrees of freedom necessary for a solution in advance: Even in the moderate post-bifurcation regime, where nonlinear contributions govern the amplitude of the deformation patterns, the wavelengths are predominantly determined
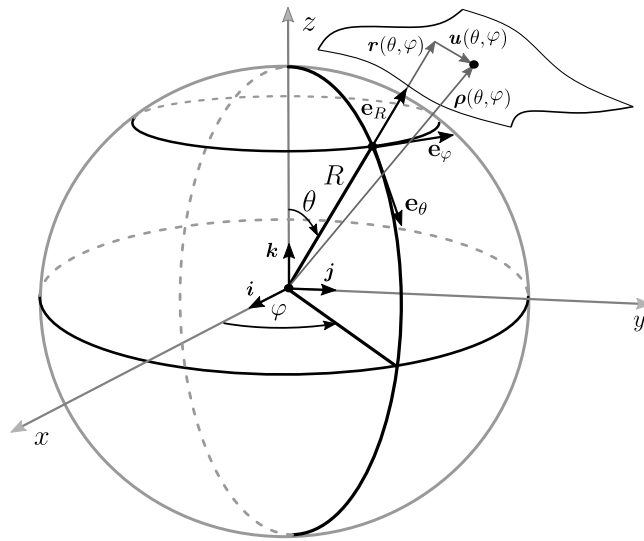
Fig. 1. The sketch shows the coordinates, the undeformed and the deformed configuration of the shell.

by the linear contributions of bending and substrate straining. Consequently, only a small subset of the spherical harmonic functions contribute to the solution, which further reduces the number of degrees of freedom required. For example, if a certain ratio of bending stiffness-to-substrate stiffness leads to a certain number wrinkles around the equator, only spherical harmonic functions with the degree of this number contribute to the deformation pattern. The approximate wavelength of the deformation patterns is well documented in the literature and can be pre-computed.

Despite these advantages, the search for the energy-minimizing equilibrium deformation field remains a challenging problem. To improve the robustness of the solution procedure, we have transformed the problem into a large-scale Quadratically Constrained Quadratic Programming (QCQP) problem, which we solve using the standard Newton-Raphson and BFGS quasi-Newton method with a line search backtracking. Compared to the path-following techniques, the energy minimization scheme is significantly more robust due to the line search and, in the case of the BFGS method, only requires an approximation of the Hessian matrix instead of a full, computationally expensive Hessian matrix [23,24]. Moreover, the QCQP method is faster and more robust than the dynamic-relaxation methods because it is able to identify and iterate in the direction of the largest negative curvature in the energy landscape, and its line-search backtracking, which optimizes iteration step length to sufficiently lower the potential energy. We demonstrate that our theory, solved numerically, can directly predict the deformation patterns observed in our experiments.

The rest of the manuscript is structured as follows: In Section 2, a new version of the shell theory for wrinkling is presented incorporating the contributions of the tangential displacements and an exact closed form solutions for the contribution of the substrate. The spectral method, which uses spherical harmonic functions as a basis, is described in detail in Section 3. In Section 4, the numerical results are presented and discussed. Finally, concluding remarks are presented in Section 5.

2. Theory

Here, we present our new theory based on Kirchhoff–Love shell assumptions. We focus on a spherical manifold, since it then naturally corresponds to the spherical harmonic functions used to represent the deformation field. The spherical harmonic functions are desirable because they do not give rise to numerically induced nucleation points due to meshing. Since they are shown to be rotationally invariant when the truncation is triangular, they do not suffer from the singularities at the poles. Finally, we show how the spherical harmonic functions are used to analytically represent the mechanical response of the substrate to deformation.

2.1. Reduced Kirchhoff–Love shell theory

We start with a smooth $\mathbb{R}^2$ surface embedded in a $\mathbb{R}^3$ space in which the position vector in the spherical coordinate system is given by $\boldsymbol{R}(\theta, \varphi) = R\boldsymbol{e}_R(\theta, \varphi)$. Here R is the radius, $\theta \in [0, \pi]$ is the polar angle and $\varphi \in [0, 2\pi]$ is the azimuthal angle, as shown in Fig. 1. Furthermore, $\boldsymbol{e}_R$ is a unit vector in the radial direction, $\boldsymbol{e}_\theta$ is a unit vector in the polar direction, and $\boldsymbol{e}_\varphi$ is a unit vector in the azimuthal direction.

For the deformed surface we construct a parametrization in the form

$$\boldsymbol{\rho}(\theta, \varphi) = r(\theta, \varphi)\boldsymbol{e}_R + u_\theta(\theta, \varphi)\boldsymbol{e}_\theta + u_\varphi(\theta, \varphi)\boldsymbol{e}_\varphi,$$

where R is the radius of the sphere in the initial configuration and u_θ and u_φ are the tangential displacements in the undeformed frame. In this way, the position vector can be decomposed as $\boldsymbol{\rho} = \boldsymbol{r} + \boldsymbol{u}$ into a component representing the radial displacement

$r = r(\theta, \varphi)e_R(\theta, \varphi)$, which is usually considered e.g. in [2,8,9], and a component that determines the radial tangential displacements $u = u_\theta(\theta, \varphi)e_\theta + u_\varphi(\theta, \varphi)e_\varphi$. This second component u largely contributes to the relaxation of the membrane stresses, but is usually neglected as its consideration requires to solve an additional stress equilibrium in the tangential direction.

The tangent tensor $\mathbf{t}$, which is also known as a deformation gradient of the deformed surface is defined as $\mathbf{t} = \nabla\rho = \nabla r + \nabla u$, where the operator ∇ represents a surface gradient of a vector in the spherical frame. Therefore the columns of the deformation gradient represent the tangent vectors of the surface. This means that for a spherical shell $\mathbf{t} = \mathbf{I}$, where $\mathbf{I}$ is a unit tensor, and when the surface deviates from the sphere, the tangent tensor changes. The right Cauchy–Green strain tensor that measures the in-plane strains connected to the deviations from the spherical surface is symmetric and is calculated as $\mathbf{C} = \mathbf{t}^T \cdot \mathbf{t} = (\nabla r)^T \cdot \nabla r + (\nabla u)^T \cdot \nabla r + (\nabla r)^T \cdot \nabla u + (\nabla u)^T \cdot \nabla u$, where $(\ )^T$ is the transposition operator. We assume that the displacement in the direction of the initial radius $w := r - R$ is at least one order of magnitude larger than the magnitude of the tangential displacements $\|u\|$, therefore assuming that $(\nabla u)^T \cdot \nabla u \approx \mathbf{0}$ and $\nabla u \cdot \nabla r \approx \nabla u \cdot \mathbf{I} = \nabla u$. With these assumptions, the right Cauchy–Green strain tensor $\mathbf{C}$ is now linear with respect to the tangential displacements u and fully nonlinear with respect to the larger radial displacements w and therefore also with respect to the radius r. It can be written as

$$\mathbf{C} = (\nabla r)^T \cdot \nabla r + (\nabla u)^T + \nabla u. \tag{1}$$

Next, we assume that right Cauchy–Green tensor is close to identity matrix and therefore the change in the metric is small. With that the curvature tensor is given by $\mathbf{b} = n \cdot \nabla\nabla\rho$, where n is a normalized surface normal. Since we consider a moderate post-bifurcation regime in which the magnitude of the tangential displacements $\|u\|$ is much smaller than that of the radial direction w and since it was shown in [8] that when using a linearized version of the bending instead of a fully nonlinear expression the associated error is insignificant for moderate deformations, we consider the linear version of the curvature tensor

$$\mathbf{b} = N \cdot \nabla\nabla r = \nabla\nabla r - \frac{r}{R^2}\mathbf{I}, \tag{2}$$

where N is a surface normal of the undeformed shell, similar to [2,8]. This allows us to calculate both the in-plane Green–Lagrange strain and the change in curvature

$$E^{\mathrm{rKL}} = \frac{1}{2}(\mathbf{C} - \mathbf{I}) \quad \text{and} \quad \kappa = \mathbf{b} - \mathbf{B}, \tag{3}$$

respectively. In terms of radial position vector magnitude r and tangential displacements they can be rewritten as

$$E^{\mathrm{rKL}} = \frac{1}{2}\left(\nabla u + (\nabla u)^T\right) + \frac{1}{2}\left((\nabla r)^T \cdot \nabla r - \mathbf{I}\right), \tag{4}$$

$$\kappa = \nabla\nabla r - \frac{r - R}{R^2}\mathbf{I}. \tag{5}$$

Now, we employ the Kirchhoff–Love shell assumptions that are valid for thin shells and relate the membrane forces and bending moments to the strains and the change in curvature, using isotropic linear elastic relations. With this the membrane forces and bending moments can be written as

$$\mathbf{N} = \mathbb{C} : E^{\mathrm{rKL}} = C\left(\nu\,\mathrm{tr}(E^{\mathrm{rKL}})\mathbf{I} + (1 - \nu)\,E^{\mathrm{rKL}}\right), \tag{6}$$

$$\mathbf{M} = \mathbb{D} : \kappa = D\left(\nu\,\mathrm{tr}(\kappa)\mathbf{I} + (1 - \nu)\kappa\right) \tag{7}$$

respectively. Here we denote the Poisson's ratio, membrane stiffness and bending stiffness with ν, $C = Eh/(1 - \nu^2)$ and $D = Eh^3/(12(1 - \nu^2))$, respectively. With E and h we denote Young's modulus and the thickness of the shell, [25].

We also consider the effects of a linearly elastic substrate by adding its potential energy $\Pi_{\mathrm{substrate}}$ to the classical Kirchhoff–Love shell energy functional Π. Here for computational efficiency and because this approximation yields quite good results [26,27], we assume that the potential energy of the substrate only depends on the radial shell displacement r. This yields the potential energy functional

$$\Pi = \frac{1}{2}\int_\Omega \kappa(r) : \mathbb{D} : \kappa(r) + E^{\mathrm{rKL}}(r, u) : \mathbb{C} : E^{\mathrm{rKL}}(r, u)\,d\Omega + \Pi_{\mathrm{substrate}}(r), \tag{8}$$

where $\Omega = [0, \pi] \times [0, 2\pi]$ and $d\Omega = R^2 \sin\theta d\theta d\varphi$. Arranging the terms leads to

$$\Pi = \frac{1}{2}\int_\Omega D\left(\mathrm{tr}(\kappa)^2 - 2(1 - \nu)\det(\kappa)\right) + C\left(\mathrm{tr}(E^{\mathrm{rKL}})^2 - 2(1 - \nu)\det(E^{\mathrm{rKL}})\right)\,d\Omega + \Pi_{\mathrm{substrate}}(r). \tag{9}$$

Its variation with respect to u results in a condition that requires the membrane stress tensor to be divergence-free. This takes the form of an equilibrium condition for the forces in the plane $\nabla \cdot \left(\mathbb{C} : E^{\mathrm{rKL}}(r, u)\right) = \nabla \cdot \mathbf{N}(r, u) = 0$.

Instead of solving this for u in terms of r, we construct a divergence-free tangential force field $\mathbf{N}$ from an Airy-like stress function ϕ. The construction of $\mathbf{N}$ is similar to the construction of the Einstein tensor in the theory of general relativity [28], which is also divergence-free. We therefore define

$$\mathbf{N} := C\left(\tilde{\nabla}\tilde{\nabla}\phi + \frac{\phi}{R^2}\mathbf{I}\right), \tag{10}$$

where $\tilde{\nabla}\tilde{\nabla}\phi = \Delta\phi\mathbf{I} - \nabla\nabla\phi$ is the adjugate of $\nabla\nabla\phi$ and Δ is the Laplace–Beltrami operator. Such a membrane force tensor $\mathbf{N}$ is divergence-free and the tangential force equilibrium is automatically satisfied. Please also note that if the tangential traction

of the substrate is also included in the formulation, this would modify the divergence free condition to a different condition, e.g., $\nabla \cdot \mathbf{N} = \boldsymbol{f}(r, \boldsymbol{u})$. Also such problem can be solved by modifying the stress function, see e.g. [29]. However, this is not the scope of our study, as it was shown in [26,27], that these contributions can be neglected in the case of wrinkling.

The stress function ϕ is not arbitrary, because it must allow the strains to satisfy the conditions of integrability/compatibility. The condition of integrability of the strains is usually given by the condition that the Ricci curvature tensor $\mathcal{R}$ of the manifold must be proportional to the Gaussian curvature of this manifold $\mathcal{K}$, see [30], i.e

$$\mathcal{R} = \mathcal{K} \, \mathbf{I}, \tag{11}$$

where $\mathcal{K} = \det(\mathbf{b})$. The Ricci curvature is a contraction of the Riemann curvature tensor can be calculated from the metric tensor $\mathbf{g} = \mathbf{C}^{1/2} \mathbf{G} \mathbf{C}^{1/2}$, with $\mathbf{G}$ being the undeformed metric. It is interesting to note that in local tangential coordinates, where the metric is locally a unit matrix and the Christoffel symbols vanish [31], the expression for the Ricci curvature is simply given by

$$\mathcal{K} = \mathcal{R}_1^1 = -\mathrm{tr}\left(\tilde{\nabla}_{||}\tilde{\nabla}_{||}\mathbf{C}\right). \tag{12}$$

Here the operator $\tilde{\nabla}_{||}\tilde{\nabla}_{||}$ is the same as defined under Eq. (10). Now we, approximate the local coordinates with the local coordinates of the sphere and apply the operation $\mathrm{tr}\left(\tilde{\nabla}\tilde{\nabla}(\ )\right)$ to the Hooke's law for the membrane strains $-(\mathbf{C} - \mathbf{I})/2 = -\mathbf{C}^{-1} : \mathbf{N} = -\mathbf{C}^{-1} : \left(\tilde{\nabla}\tilde{\nabla}\phi + \phi/R^2\mathbf{I}\right)$ and obtain the condition on the stress function as

$$\Delta^2 \phi - \frac{2(1-\nu)\phi}{R^4} = -\frac{1}{2}\left(\det(\mathbf{b}) - \frac{1}{R^2}\right). \tag{13}$$

Now inserting our linearized expression for the curvature from Eq. (2) we obtain

$$\Delta^2 \phi - \frac{2(1-\nu)\phi}{R^4} = -\frac{1}{2}\left(\frac{\nabla\nabla r : \tilde{\nabla}\tilde{\nabla} r}{2} - \frac{r\Delta r}{R^2} + \frac{r^2 - R^2}{R^4}\right), \tag{14}$$

where $\nabla\nabla r : \tilde{\nabla}\tilde{\nabla} r/2 = \det(\nabla\nabla r)$.

Since the potential energy can also be written in terms of membrane stresses, we can use the definition of the stress function given in Eq. (10) and the definition of the curvature given in Eq. (2) to write the potential energy of the structure as

$$\begin{aligned}
\Pi = \frac{1}{2}\int_\Omega &D\left(\left(\Delta r - \frac{2r - 2R}{R^2}\right)^2 - 2(1-\nu)\det\left(\nabla\nabla r - \frac{r - R}{R^2}\mathbf{I}\right)\right) + \\
&+ C\left(\left(\Delta\phi + \frac{2\phi}{R^2}\right)^2 - 2(1+\nu)\det\left(\tilde{\nabla}\tilde{\nabla}\phi + \frac{\phi}{R^2}\mathbf{I}\right)\right) d\Omega + \\
&+ \Pi_{\mathrm{substrate}}(r).
\end{aligned} \tag{15}$$

Mind that although the potential is quadratic (linear problem) in the variables r and ϕ, considering ϕ is a quadratic function of r the problem is altogether nonlinear.

Because the term $(r - R)/R^2$ is negligible compared to the term $\nabla\nabla r$, unless the wavelength of the deformation pattern is similar to the radius R, see [2], we will neglect it with minimal loss of accuracy. Since now on a sphere $\int_\Omega \det(\nabla\nabla f)\, d\Omega = \int_\Omega -\Delta f/(2R^2)d\Omega$, where f is a scalar function and because $\det\left(\nabla\nabla\phi + \phi/R^2\mathbf{I}\right) = \det(\nabla\nabla\phi) + \Delta\phi\phi/R^2 + \phi/R^4$, the total elastic energy can be rewritten in the form of the Laplace–Beltrami operator Δ on the unknown scalar functions r and ϕ in the shell energy. This greatly simplifies the final system of equations, since Δf is easy to evaluate on a surface of a sphere using spherical harmonic functions. The strain energy is now

$$\begin{aligned}
\Pi = \frac{1}{2}\int_\Omega &D\left((\Delta r)^2 + 2(1-\nu)\frac{r\Delta r}{2R^2}\right) + \\
&+ C\left(\left(\Delta\phi + \frac{2\phi}{R^2}\right)^2 - 2(1+\nu)\left(-\frac{\phi\Delta\phi}{2R^2} + \frac{\phi^2}{R^4}\right)\right) d\Omega + \Pi_{\mathrm{substrate}}(r).
\end{aligned} \tag{16}$$

If we assume that the substrate is a linear elastic solid, the quadratic functional in Eq. (16) and the quadratic constraint in Eq. (14) form a Quadratically Constrained Quadratic optimization Problem (QCQP), which can be solved using existing large-scale optimizers.

2.2. Contribution of the substrate

Because we will use the spherical harmonic functions to represent the functions on the sphere, we can model the substrate as an isotropic linear elastic solid, for which there exist explicit analytical relations in terms of the spherical harmonic functions between the displacements and the traction's on the boundary of the substrate. With that the substrate model is solved accurately without an additional computational cost, contrary to the Winkler-type heuristic approach.

Let us now consider a (solid) ball, where the displacements at the center are zero. The displacements of the substrate are given in the frame of the radial $\boldsymbol{S}_r$, tangential $\boldsymbol{S}_g$ and binormal directors $\boldsymbol{S}_b$, given by a vector spherical harmonic functions [32]. Therefore, the displacement component of spherical harmonic degree l and order m are given by

$$(\boldsymbol{u}_g)_l^m = R^{l-1}\left((\boldsymbol{S}_g)_l^m + l(\boldsymbol{S}_r)_l^m\right) \tag{17}$$

$$(\boldsymbol{u}_r)_l^m = R^{l+1}\left(\beta_l(\boldsymbol{S}_g)_l^m + \gamma_l(\boldsymbol{S}_r)_l^m\right). \tag{18}$$

Here, R is the outer radius, $\beta_l = (l + 5 - 4\nu_s)/((l + 1)(2l + 3))$ and $\gamma_l = (l - 2 + 4\nu_s)/(2l + 3)$. Furthermore, the traction vector in the radial direction is given by

$$(\boldsymbol{T}_r)_l^m = 2\mu_s R^l \left(b_l (\boldsymbol{S}_g)_l^m + g_l (\boldsymbol{S}_r)_l^m \right), \tag{19}$$

where μ_s is the shear modulus of the substrate, $b_l = (l+1)\beta_l - 2(1-\nu_s)/(l+1)$ and $g_l = (l+1)\gamma_l - 2\nu_s$. Here, $\boldsymbol{S}_g$ and $\boldsymbol{S}_r$ can be eliminated by the assumption that only the prescribed normal displacements $(\boldsymbol{u}_r)_l^m = (r - R)_l^m \boldsymbol{e}_R$ are non-zero, while tangential displacements on the surface of the substrate are zero, i.e. $(\boldsymbol{u}_r)_l^m = \boldsymbol{0}$. Therefore,

$$(\boldsymbol{T}_r)_l^m = \frac{2\mu_s}{R} \frac{g_l - l b_l}{\gamma_l - l \beta_l} (r - R)_l^m \boldsymbol{e}_R. \tag{20}$$

Expression $(r - R)_l^m = \int_\Omega (r - R) \overline{Y}_l^m \, d\Omega$ represents the amplitudes of the spherical harmonic transformation of the radial displacements, where Y_l^m are scalar spherical harmonic functions and $\overline{Y}_l^m$ are its complex conjugates. Since the substrate is linearly elastic, the strain energy of the linear elastic substrate can be written as

$$\Pi_{\text{substrate}} = \frac{1}{2} \int_\Omega \sum_{l,m}^\infty \frac{2\mu_s}{R} \frac{g_l - l b_l}{\gamma_l - l \beta_l} (r - R)_l^m (r - R)_l^m Y_h^n \overline{Y}_l^m \, d\Omega. \tag{21}$$

3. Galerkin spectral method using spherical harmonics

In the Galerkin spectral method, functions are represented using a basis of orthogonal polynomials. Specifically, in our approach, functions are expressed as an infinite series of weighted spherical harmonic functions

$$f(\theta, \varphi) = \sum_{l=0}^\infty \sum_{m=-l}^l A_l^m Y_l^m(\theta, \varphi), \tag{22}$$

where A_l^m is the weight or the amplitude of a certain spherical harmonic function $Y_l^m(\theta, \varphi)$ with degree l and order m. The main advantage of this method lies in its extremely fast convergence for smooth functions [21,22,33], as this provides a relatively low number of degrees of freedom compared to, e.g., the finite element method, and thereby enables the use of direct energy minimization methods. By employing a triangular truncation of the infinite spherical harmonic series with $l \leq l_{\max}$, the function retains rotational invariance, ensuring no loss of generality or any bias at the poles due to truncation, [21,34].

This approach translates the problem from solving a system of differential equations to solving a system of algebraic equations. This eliminates the need for spatial discretization, thus avoiding issues with singularities at the poles of the spheres and removes spurious non-physical nucleation points for wrinkle evolution, which arise in the classical numerical methods, since, e.g., a sphere cannot be discretized symmetrically according to the *Gauss–Bonnet theorem*.

Spectral methods utilizing orthogonal polynomials are well-known for their rapid convergence [22]. Combined with their the banded nature of the deformation patterns in wrinkling, and its fast convergence without spatial discretization bias, these methods appear to be optimal for this type of problem.

Unfortunately, the method has some drawbacks. Firstly, applying Galerkin spectral methods to problems on complex domains, with intricate boundary conditions or spatially varying coefficients, is challenging because they generate highly coupled systems of equations characterized by difficult-to-handle discrete convolution terms [21,22,33]. Fortunately, our problem does not contain any spatially varying properties and is defined on a closed spherical domain $\Omega = [0, \pi] \times [0, 2\pi]$ (without an edge $\partial\Omega$), but it does include nonlinear terms, which also generate coupled nonlinear systems of equations characterized by discrete convolution operations. To address this problem, we use a variant of the Galerkin spectral methods, the Galerkin pseudo-spectral method. Instead of resolving the convolution operation directly, we use the Fast Spherical Fourier Transform to convert the nonlinear terms into physical space, where the convolution operation becomes a simple pointwise multiplication. We then transform the product back into the space of spherical harmonics. This approach preserves all the advantageous convergence properties of the spectral method [21,33].

An alternative approach would be to use spectral collocation methods. In this approach, the functions are represented by their values at the integration points in physical space. Although this makes it easier to deal with non-linear operators and spatially varying coefficients, differential operations require interpolation of the function for differentiation. This interpolation is achieved by representing the functions by a spherical polynomial using the inverse Fast Spherical Fourier Transform to obtain the amplitudes of the spherical harmonic function interpolation. Differential operations are then performed on the interpolation function and the values at the integration points in physical space are again determined using the Fast Spherical Fourier Transform. Although spectral collocation methods are simpler and somewhat easier to implement than spectral Galerkin methods, they suffer from aliasing problems and do not have the advantages mentioned above. For these reasons, we opt for the more challenging-to implement Galerkin spectral method [33].

Although there exist some implementations of Galerkin spectral methods on a sphere that use spherical harmonics, such as those used in meteorology [35], we could not find a suitable one for solving a fourth-order system of PDEs as required for our problem. Therefore, we developed our own code in `Matlab` [36].

3.1. The spherical harmonic basis

The basis functions for our harmonic approximation are the spherical harmonic functions $Y_l^m(\theta, \varphi)$ of an integer degree $l \geq 0$ and integer order $-l \leq m \leq l$. These are complex functions that are defined as solutions of the Laplace equation $\Delta f = 0$ in the spherical coordinate system or a Helmholtz problem on the surface of a unit sphere $\Delta Y_l^m + l(l+l)Y_l^m = 0$. Using the normalization commonly used in quantum mechanics, the spherical harmonic functions are given as

$$Y_l^m(\theta, \varphi) = (-1)^m \sqrt{\frac{(2l+1)}{4\pi} \frac{(l-m)!}{(l+m)!}} P_l^m(\cos\theta) e^{im\varphi}, \tag{23}$$

where $P_l^m(\cos\theta)$ are the associated Legendre polynomials which are defined as

$$P_\ell^m(x) = \left(1 - x^2\right)^{m/2} \frac{d^m}{dx^m} \left(P_\ell(x)\right). \tag{24}$$

Here, $P_n(x)$ are the classical Legendre polynomials, which are defined by

$$P_n(x) = \frac{1}{2^n n!} \frac{d^n}{dx^n} \left(x^2 - 1\right)^n. \tag{25}$$

For more details see e.g. [37–40]. The Spherical harmonic functions form a complete and orthogonal basis on the surface of a sphere with

$$\int_0^{2\pi} \int_0^{\pi} Y_l^m(\theta, \varphi) \overline{Y}_h^n(\theta, \varphi) \sin\theta d\theta d\varphi = \delta_l^h \delta_m^n, \tag{26}$$

where $\overline{Y}_h^n(\theta, \varphi)$ is the complex conjugate of $Y_h^n(\theta, \varphi)$ and δ_l^h and δ_m^n are Kronecker delta functions. Therefore, a scalar function on a sphere can be represented as an infinite sum

$$f(\theta, \varphi) = \sum_{l=0}^{\infty} \sum_{m=-l}^{l} A_l^m Y_l^m(\theta, \varphi) \tag{27}$$

with A_l^m being complex amplitudes of the complex spherical harmonics
$A_l^m = \int_0^{2\pi} \int_0^{\pi} f(\theta, \varphi) \overline{Y}_l^m(\theta, \varphi) \sin\theta d\theta d\varphi$. Because we deal with functions, which are smooth, meaning they are mainly composed of lower degree spherical harmonic function, a band-limited series approximate

$$f_{\text{band limited}}(\theta, \varphi) = \sum_{l=0}^{l_{\max}} \sum_{m=-l}^{l} A_l^m Y_l^m(\theta, \varphi) \tag{28}$$

is quickly convergent. More about the convergence can be seen in Section 4.1. Since the spherical harmonic functions are usually displayed in a 3D representation with integer values $l \geq 0$ on the horizontal axis, integer values $-l \leq m \leq l$ on the vertical axis and the magnitudes of the coefficients A_l^m in the out-of-plane axis, such $l \leq l_{\max}$ is usually referred to as triangular truncation. It is invariant to rotations and does not produce nonphysical values of the function at the poles, as is the case with other types of truncation [34,41].

The surface gradient of a scalar function written in the form of spherical harmonic functions $f(\theta, \varphi) = \sum_{l=0}^{l_{\max}} \sum_{m=-l}^{l} A_l^m Y_l^m(\theta, \varphi)$, which will from now on be denoted by $\nabla f = f_{,\theta} e_\theta + f_{,\varphi}/\sin\theta e_\varphi$, where $f_{,\theta} = \partial f/\partial\theta$ and $f_{,\varphi} = \partial f/\partial\varphi$. If we combine different recurrence relations (see [42–44]) valid for spherical harmonic functions the gradient can be written as an algebraic expression of other spherical harmonic functions as

$$\nabla f = \sum_{l,m} A_l^m \nabla Y_l^m = f_{,\theta} e_\theta + \frac{f_{,\varphi}}{\sin\theta} e_\varphi = \tag{29}$$

$$= \sum_{l,m} A_l^m \left(\frac{e^{i\varphi} \sqrt{l(l+l) - m(m-1)}}{2} Y_l^{m-1} + \frac{e^{-i\varphi} \sqrt{l(l+l) - m(m+1)}}{2} Y_l^{m+1} \right) e_\theta$$

$$- i \sum_{l,m} A_l^m \sqrt{\frac{(2l+1)}{4(2l-1)}} \left(e^{i\varphi} \sqrt{(l+m-1)(l+m)} Y_{l-1}^{m-1} + e^{-i\varphi} \sqrt{(l-m-1)(l-m)} Y_{l-1}^{m+1} \right) e_\varphi.$$

Here, we have denoted $\sum_{l=0}^{l_{\max}} \sum_{m=-l}^{l}$ as $\sum_{l,m}$. Note that this allows us to easily compute the gradient of a scalar function in physical space, but the expression for the gradient in function space requires an additional transformation from the physical to the function space. To our knowledge, the gradient directly in function space is only given in a 3D Cartesian frame and not in the spherical frame, see [37,38].

On the other hand, the calculation of the Laplace–Beltrami operator acting on a scalar function is almost trivial, since the spherical harmonic functions are defined by $\Delta f = 0$ and with that

$$\Delta f = \sum_{l,m} A_l^m \Delta Y_l^m = \sum_{l,m} -l(l+1) A_l^m Y_l^m. \tag{30}$$

Finally, we define the Hessian of a scalar function $\nabla\nabla f =: H_{\theta\theta} e_\theta \otimes e_\theta + H_{\theta\varphi} e_\theta \otimes e_\varphi + H_{\varphi\theta} e_\varphi \otimes e_\theta + H_{\varphi\varphi} e_\varphi \otimes e_\varphi$. The component $H_{\theta\theta}$ can be computed as

$$
\begin{aligned}
H_{\theta\theta} = f_{,\theta\theta} = \sum_{l,m} A_l^m \Bigg(&\frac{1}{2}\left(-l^2 - l + m^2\right) Y_l^m + \\
&+ \frac{1}{4}e^{2i\varphi}\sqrt{(l-m-1)(l-m)(l+m+1)(l+m+2)} Y_l^{m-2} \\
&+ \frac{1}{4}e^{-2i\varphi}\sqrt{(l-m+1)(l-m+2)(l+m-1)(l+m)} Y_l^{m+2} \Bigg)
\end{aligned}
\tag{31}
$$

and the off-diagonal component $H_{\theta\varphi} = H_{\varphi\theta}$ is

$$
\begin{aligned}
H_{\theta\varphi} = \frac{f_{,\theta\varphi}}{\sin\theta} - \frac{\cot\theta f_\varphi}{\sin\theta} = -i\sum_{l,m} A_l^m \Bigg(&m\left(lm + m^2 - 1\right)\sqrt{\frac{(2l+1)\left(l^2 - m^2\right)}{4(2l-1)\left(m^2 - 1\right)^2}} Y_{l-1}^m + \\
&+ e^{2i\phi}\sqrt{\frac{(2l+1)(l+m-2)(l+m-1)\left(l^2 + l - m^2 + m\right)}{16(2l-1)(m-1)^2}} Y_{l-1}^{m-2} + \\
&+ (2m+1)e^{-2i\phi}\sqrt{\frac{(2l+1)\left(l^2 + l - m(m+1)\right)\left(l^2 - l(2m+3) + m^2 + 3m + 2\right)}{16(2l-1)(m+1)^2}} Y_{l-1}^{m+2} \Bigg).
\end{aligned}
\tag{32}
$$

The final component $H_{\varphi\varphi}$ can be expressed with the use of the relations $H_{\varphi\varphi} = \Delta f - H_{\theta\theta}$, where Δf can be computed from Eq. (30).

3.2. Total energy of the system in the function space

Now including the contribution of the substrate in Eq. (21) the total strain energy of the system in Eq. (16), can be written as

$$
\begin{aligned}
\Pi = \sum_{l,m} \Bigg(&\frac{D}{2R^4}\left((-l(l+1))^2 - 2(1-\nu)l(l+1)\right)\left(\hat{r}_l^m\right)^2 + \frac{2\mu_s}{R}\frac{g_l - lb_l}{\gamma_l - l\beta_l}(\hat{r}_l^m - \hat{R}_l^m)^2 \\
&+ \frac{C}{2R^4}\left((-l(l+1)+2)^2 - 2(1+\nu)\left(\frac{l(l+1)}{2}+1\right)\right)\left(\hat{\phi}_l^m\right)^2\Bigg)R^2.
\end{aligned}
\tag{33}
$$

With $\hat{r}_l^m$, $\hat{R}_l^m$ and $\hat{\phi}_l^m$ being amplitudes of spherical harmonic expansion of $r(\theta,\varphi)$, R and $\phi(\theta,\varphi)$, respectively. Because R is a constant, the expansion only has one non-zero component $\hat{R}_0^0 = \sqrt{4\pi}R$, where the factor $\sqrt{4\pi}$ comes from the normalization of the spherical harmonic functions. The energy can be written in the quadratic form as

$$
\Pi = \frac{1}{2}u^T \mathbf{H} u.
\tag{34}
$$

Here, u, $(u)^T = (r^T, \hat{\phi}^T)$, is stacked vector of the amplitudes with $\hat{r} := (\hat{r}_l^m)$ and $\hat{\phi} := (\hat{\phi}_l^m)$, while $\mathbf{H}$ is a diagonal stiffness matrix and at the same time the Hessian matrix of the system, which is block diagonal with $\mathbf{H} = \text{diag}\left(\mathbf{H}_r, \mathbf{H}_\phi\right)$. Both sub-matrices $\mathbf{H}_r$ and $\mathbf{H}_\phi$ are diagonal, and contain the bending/substrate contributions and the membrane stress contributions, respectively.

3.3. The constraint in the function space

The constraint in Eq. (14) is more problematic because the transformation into the spherical harmonic space results in the following $(l_{\max} + 1)^2$ constraints, which are given by

$$
\frac{1}{R^4}\frac{l^2(l+1)^2 - 2(1-\nu)}{R^4}\hat{\phi}_l^m + \frac{1}{2}\left(\frac{1}{2}S\left(\nabla\nabla r : \tilde{\nabla}\tilde{\nabla}r\right)_l^m - S\left(\frac{r\Delta r}{R^2}\right)_l^m + S\left(\frac{r^2 - R^2}{R^4}\right)_l^m\right) = 0
\tag{35}
$$

with $S(f)_l^m = \hat{f}_l^m$ being the spherical transform operator.

An advantage of the Galerkin spectral method is that we can enforce a direct control of the average shell radius normalized to the initial radius of the wrinkled sphere $\lambda := r_{\text{avg}}/R = \int_\Omega r\, d\Omega/R$. If we decompose the radius r into the average radius and the varying part of the radius $r(\theta,\varphi) = \lambda R + r_{\text{var}}(\theta,\varphi)$ this means that the transform coefficients $S(r)_l^m$ can be written as $S(r)_0^0 = \int_\Omega r(\theta,\varphi)d\Omega/\sqrt{4\pi} = \sqrt{4\pi}\lambda R$ for the 0-th coefficient and $S(r)_{l>0}^m = S(r_{\text{var}})_{l>0}^m$ for the higher order and degree coefficients. Similarly, the term $S(r^2)_0^0$ from Eq. (35) can be decomposed into

$$
S(r^2)_0^0 = \frac{1}{\sqrt{4\pi}}\int_\Omega \lambda^2 R^2 + 2\lambda R r_{\text{var}}(\theta,\varphi) + r_{\text{var}}(\theta,\varphi)^2 d\Omega.
\tag{36}
$$

Using the generalized Parseval's theorem for spherical harmonics [41], $\int_\Omega r_{\text{var}}(\theta,\varphi)^2 d\Omega = \sum_{l=1}^{l_{\max}}\sum_{m=-l}^{m=l}\hat{r}_l^m\overline{\hat{r}_l^m}$ and the fact that by construction $\int_\Omega r_{\text{var}}(\theta,\varphi)d\Omega = 0$ it follows that

$$
S(r^2)_0^0 = \sqrt{4\pi}\lambda^2 R^2 + \sum_{l=1}^{l_{\max}}\sum_{m=-l}^{m=l}\hat{r}_l^m\overline{\hat{r}_l^m}.
\tag{37}
$$

With this the average radius $r_{\text{avg}} = \lambda R$ can be directly prescribed in the constraints in Eq. (35) in the term

$$S\left(\frac{(r^2 - R^2)}{R^4}\right)_0^0 = \sqrt{4\pi}\left(\frac{\lambda^2 - 1}{R^2}\right) + \sum_{l=1}^{l_{\max}} \sum_{m=-l}^{m=l} \frac{\hat{r}_l^m \overline{\hat{r}_l^m}}{R^4}. \tag{38}$$

Therefore, the first Eq. in Eqs. (35) can be written as

$$\frac{-2(1 - \nu)\hat{\phi}_0^0}{R^4} + \frac{1}{2}\left(\frac{1}{2}S\left(\nabla\nabla r : \tilde{\nabla}\tilde{\nabla}r\right)_0^0 - S\left(\frac{r\Delta r}{R^2}\right)_0^0 + \sqrt{4\pi}\left(\frac{\lambda^2 - 1}{R^2}\right) + \sum_{l=1}^{l_{\max}} \sum_{m=-l}^{m=l} \frac{\hat{r}_l^m \overline{\hat{r}_l^m}}{R^4}\right) = 0, \tag{39}$$

where λ can be directly used to control the average radius of the deformed shell.

Similar to the total potential energy, the constraints can be rewritten in a more compact matrix form

$$\frac{1}{2}\boldsymbol{u}^T \mathbb{Q}\boldsymbol{u} + \mathbf{L}\boldsymbol{u} + \boldsymbol{R} = \mathbf{0}, \tag{40}$$

where $\mathbb{Q}$ is a $2n \times 2n \times 2n$ 3rd order tensor, where $n = (l_{\max} + 1)^2$. It can be represented as a 3rd order spatially block-diagonal matrix $(\mathbb{Q})_{[2n \times 2n \times 2n]} = \text{diag}\left((\mathbb{Q}_r)_{[n \times n \times n]}, (\mathbb{0})_{[n \times n \times n]}\right)$. This means, its only nonzero block component is $(\mathbb{Q}_{111})_{[n \times n \times n]} = (\mathbb{Q}_r)_{[n \times n \times n]}$, while all the other block components are zero matrices $(\mathbb{0})_{[n \times n \times n]}$. Furthermore, $\mathbf{L}$ is a 2nd order matrix $\mathbf{L} = \text{diag}\left(\mathbf{L}_r^T, \mathbf{L}_\phi^T\right)$ and $\boldsymbol{R}$ is a vector of zeros except for the first component $(\boldsymbol{R})_0^0 = \sqrt{4\pi}\left(\lambda^2 - 1\right)/R^2$. The 3rd order matrix $\mathbb{Q}$ contains quadratic contributions from the parts $S\left(\nabla\nabla r : \tilde{\nabla}\tilde{\nabla}r\right)_l^m / 2$, $S\left(((r - R\lambda)\Delta r)/R^2\right)_l^m$ and $S\left((r^2 - R^2)/R^4\right)_l^m$, while $\mathbf{L}$ is a diagonal 2nd order tensor with the contributions from the linear parts such as from $S\left(R\lambda\Delta r/R^2\right)_l^m$ and the stress function contributions $(l^2(l+1)^2 - 2(1 - \nu))/R^4 \hat{\phi}_l^m$.

Note that the vector $\hat{\boldsymbol{\phi}}$ can be expressed as a quadratic function of $\hat{r}$ using Eq. (40) and inserted into the potential energy in Eq. (34) to cut the number of degrees of freedom in half and obtaining an unconstrained quartic minimization problem. Yet, we do not do that, as such problem is much more difficult to solve than the original quadratically constrained quadratic minimization problem (QCQP).

3.4. Real spherical harmonic basis

Since most optimization programs only accept real values, we prefer to use the real versions of the spherical harmonic functions for our calculations. They are defined as

$$\mathbb{R}\left(Y_l^m\right) = \begin{cases} \frac{i}{\sqrt{2}}\left(Y_l^m - (-1)^m Y_l^{-m}\right), & \text{if } m < 0, \\ Y_l^0, & \text{if } m = 0, \\ \frac{1}{\sqrt{2}}\left(Y_l^{-m} + (-1)^m Y_l^m\right), & \text{if } m > 0 \end{cases} \tag{41}$$

with the orthogonality relation

$$\int_0^{2\pi} \int_0^\pi \mathbb{R}\left(Y_l^m(\theta, \varphi)\right) \mathbb{R}\left(Y_h^n(\theta, \varphi)\right) \sin\theta \, d\theta \, d\varphi = \delta_l^h \delta_m^n. \tag{42}$$

We can use the definition in Eq. (23) to rewrite the whole system using a simple linear transformation matrix $\mathbf{T}$ on the vector $\boldsymbol{u}$, which contains the amplitudes in the complex spherical harmonic frame with $\boldsymbol{u}_{\text{real}} = \mathbf{T} \cdot \boldsymbol{u}_{\text{complex}}$ and vice versa.

3.5. Numerical implementation

Our implementation in Matlab is roughly divided into two steps. First, in the initialization phase, the calculation of the sparse 3rd order matrix $\mathbb{Q}$ is performed. This is the most costly step of all and only needs to be carried out once for a certain number of degrees of freedom, regardless of all other material properties. Then also the diagonal $\mathbf{L}$ 2nd order matrix and the residual vector $\boldsymbol{R}$ of the quadratic constraints Eq. (40) and the 2nd order Hessian matrix $\mathbf{H}$ for the calculation of the quadratic functional in Eq. (34) are computed.

Second, with the prepared matrices $\mathbb{Q}$, $\mathbf{L}$, $\boldsymbol{R}$ and $\mathbf{H}$ an advanced algorithm is used for large-scale constraint optimization. Since the problem is large and non-convex, the algorithm must be able to detect negative curvature in the system in order to iterate to at least a meta-stable minimum energy solution for a given load parameter λ and a random initial starting solution $\boldsymbol{u}_0$.

3.5.1. First step

The structure of the matrices $\mathbf{L}$, $\boldsymbol{R}$ and $\mathbf{H}$ is more or less trivial because the matrix $\mathbf{H}$ can be explicitly extracted from the total potential energy functional in Eq. (33) as in Eq. (40) and similarly the matrix $\mathbf{L}$ and the vector $\boldsymbol{R}$ can be extracted from Eqs. (39) and (40). However, the structure of the 3rd order matrix $\mathbb{Q}_r$ is more convoluted. It is composed of the parts $\mathbb{Q}_r = \mathbb{Q}_{\text{det}} + \mathbb{Q}_{\text{tr}} + \mathbb{Q}_{r^2}$. Here, the part $\mathbb{Q}_{\text{det}}$ comes from the determinant of the curvature operation as $2\hat{r}^T \mathbb{Q}_{\text{det}}\hat{r} = S\left(\nabla\nabla r : \tilde{\nabla}\tilde{\nabla}r\right)_l^m$ since $2\det(\nabla\nabla r) = \nabla\nabla r : \tilde{\nabla}\tilde{\nabla}r$. One way to calculate this 3rd order matrix is to know the explicit expression for the multiplication and Hessian of the functions written in the spherical harmonic basis, but this is extremely complicated. For this reason, we calculate the matrix using a numerical approach. In that way the elements $Q_{\text{det},ijk}$ of the matrix $\mathbb{Q}_{\text{det}}$, where $0 \leq i, j, k \leq (l_{\max} + 1)^2$, can be computed by the transformation $Q_{\text{det},ijk} = S\left(\nabla\nabla\delta_i : \tilde{\nabla}\tilde{\nabla}\delta_j\right)_k / 2$. Here, $\delta_i = S^{-1}(\hat{\delta}_i)$ and $\delta_j = S^{-1}(\hat{\delta}_j)$ are the physical space representations of the one-dimensional Kronecker delta functions in the space of spherical harmonic functions, e.g. $\hat{\delta}_2 = (0, 1, 0, 0, \ldots, 0)$. In such way matrix

$\mathbb{Q}_{\text{det}}$ transforms $\boldsymbol{u}$ the same as $S\left(\nabla\nabla r : \tilde{\nabla}\tilde{\nabla} r\right)_l^m$. Similarly, the elements of the 3rd order matrices $\mathbb{Q}_{\text{tr}}$ and $\mathbb{Q}_{\text{r}^2}$ can be computed from $Q_{\text{tr},ijk} = S\left(\delta_i\Delta\delta_j + \delta_j\Delta\delta_i\right)_k / (2R^2)$ and $Q_{\text{r}^2,ijk} = S\left(\delta_i\delta_j\right)_k / R^4$, respectively.

Since the quadratic constraints are given by Eq. (40) it can be seen that the 3rd order matrix $\mathbb{Q}$ contains Hessian matrices of the constraints, and these are constant and only need to be calculated once. Similarly, the Hessian of the quadratic energy is constant and is exactly $\mathbf{H}$ and only needs to be calculated once. This is extremely important, as the calculation of $\mathbb{Q}$ is extremely time consuming due to the $(l_{\max}+1)^2 \times (l_{\max}+1)^2$ times that the spherical Fourier transform must be used in the calculation. Therefore, it is advantageous to use a fast spherical harmonic transform where the number of calculations for one transformation is of the order of $\sim \mathcal{O}(l_{\max}^2 \log l_{\max}^2 + M)$, where M is the number of integration nodes, which is usually similar to $l_{\max}^2$. Such an algorithm can be found in the `nfsft` implementation, which stands for the algorithm Nonequispaced fast spherical Fourier transform and is contained in the library NFFT3, which is available in [45]. The library provides algorithms for the Nonequispaced fast Fourier transform and allows the use of equispaced, Gauss–Legendre and other integration schemes, the advantages of which are well described in [46]. We note that the use of the Gauss–Legendre integration scheme is optimal as it only requires $(l_{\max}+1)^2$ integration points, while integration with an equidistant equispaced integration mesh due to aliasing requires at least $4(l_{\max}+1)^2$ nodes.

Because the spherical harmonics in the algorithm [45] are defined without the $(-1)^m$ factor (see the NFFT3 manual), we add $(-1)^m$ to the computed amplitudes of the spherical harmonic functions A_l^m to fit our definition given in Eq. (23).

3.5.2. Second step

After calculating the coefficient matrices $\mathbb{Q}$, $\mathbf{L}$, $\mathbf{H}$ and the vector $\boldsymbol{R}$, we use the nonlinear constrained non-convex optimization algorithm `IPOPT` for Matlab to minimize the total strain energy, [47,48]. The main feature of the algorithm is that it detects negative curvature in the objective function landscape and is able to take a step in that direction. This is extremely important since our problem is non-convex and therefore other, less sophisticated optimization algorithms diverge or converge to a trivial solution.

As mentioned above, another key property for the convergence of this system is that we minimize the quadratic strain energy according to both $\hat{\phi}_l^m$ and $\hat{u}_l^m$ under quadratic constraints instead of using the constraints to obtain an unconstrained optimization problem with a quartic energy, which is much more difficult to solve for several reasons. First, in the quadratic optimization problem with quadratic constraints, unlike the optimization problem with quartic energy, the Hessian matrices are constant and only need to be calculated once. Therefore, the actual optimization process is much faster. Secondly, constrained optimization is more robust and converges for almost any initial values. This is due to the fact that at the beginning of the iterative process, the constraints are still loose and the potential energy landscape is rather convex. As the constraints become tighter, the potential energy landscape slowly becomes less convex, but the algorithm can gradually converge to the candidate points for the optimum, [49–51].

Interestingly, it turns out that it is also efficient in the optimization procedure to use a quasi-Newton approximation of the Hessian matrices. In fact, this is numerically even more stable, but the solution process is somewhat longer.

4. Numerical results

In this section, we first show the convergence analysis, followed by a comparison of our results with those in the literature and our experiments. We continue by analyzing the evolution of the deformation patterns when increasing the displacement-controlled load and conclude by analyzing different calculated deformation patterns.

4.1. Convergence analysis

The entire PDE problem is reformulated as an algebraic problem and solved entirely in terms of the coefficients $\hat{r}_l^m$ and $\hat{\phi}_l^m$ from the truncated infinite series of spherical harmonic functions. Consequently, the truncation error depends on two key factors: (1) the rate of convergence of the series within the truncation limit $l_{\max}$, and (2) the extent to which the truncated coefficients influence the solution in the physical space, given that a finite series is employed.

First, we examine the method's rate of convergence and the concentration of large coefficients. It is well-established in the literature that when the spherical harmonic coefficients of the approximated function converge rapidly with increasing l, a highly accurate approximation can be achieved with a relatively small number of coefficients [41]. It seems that in our problem, the dominant modes are banded, and the coefficients exhibit rapid convergence as the distance from the band increases. This is demonstrated in Figs. 2 (a)–(c).+, where we show the deformation pattern, the amplitudes $\hat{r}_l^m$ and the amplitudes $\hat{\phi}_l^m$ of the collaborating modes in the case where the dimple pattern occurs. It is useful to know that the location of the center of the band l_{cr} of spherical harmonics where the amplitudes $\hat{r}_l^m$ are non-zero can be the theoretically predicted. Because the critical degree l_{cr} equals to the number of wrinkles counting from one pole to another the formula given by [6] can be rewritten into

$$l_{\text{cr}} = h/R \sqrt[3]{(1-v_s^2)E_f/((1-v^2)3E_s)}. \tag{43}$$

This holds for relatively large l_{cr}, where the curvature does not affect the wavelength of the dimples.

Panels (d)–(e) in Fig. 2 depict the deformation pattern, the amplitudes $\hat{r}_l^m$, and the amplitudes $\hat{\phi}_l^m$ of the corresponding modes, respectively, in the case where the load significantly exceeds the bifurcation load, resulting in a labyrinth pattern. The $\hat{r}_l^m$ amplitude spectrum in panel (e) is more dispersed but remains somewhat banded around $l_{\text{cr}} = 20$. In contrast, the $\hat{\phi}_l^m$ spectrum is concentrated around lower degree spherical harmonics.
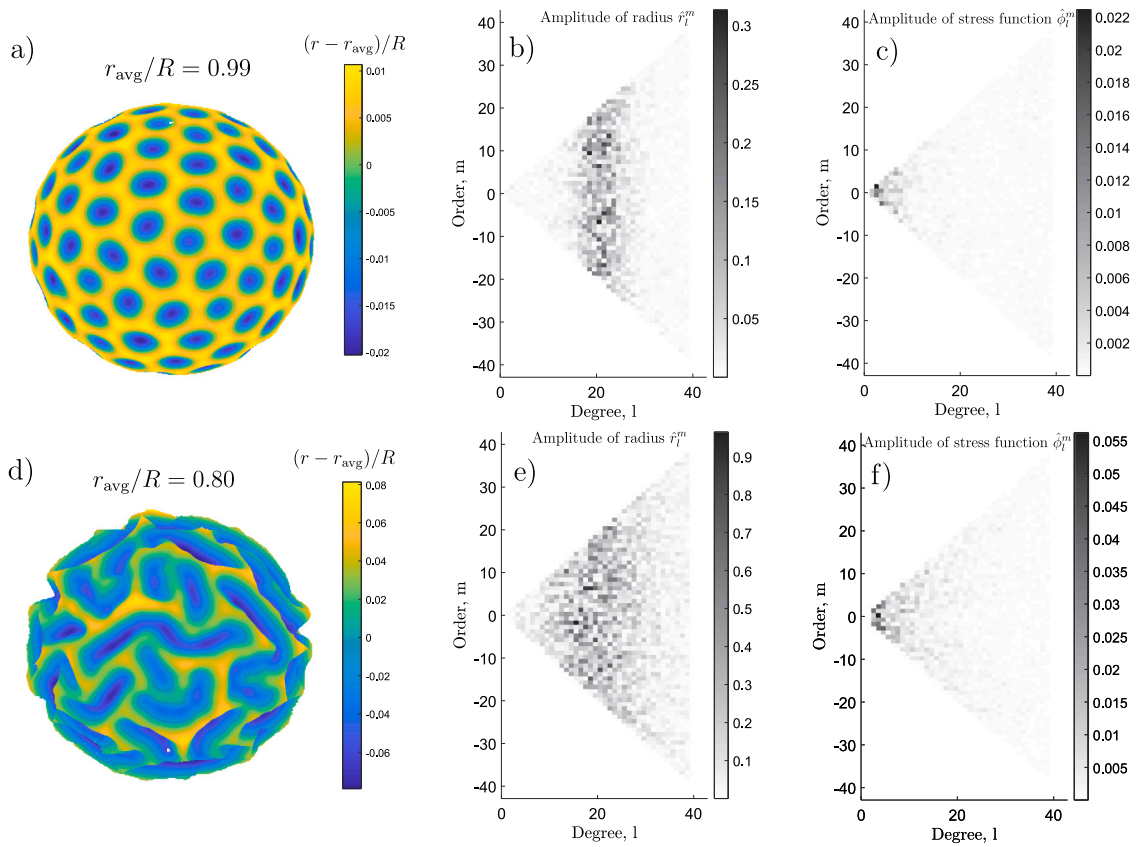
Fig. 2. The deformation patterns near and far from the bifurcation point are shown in panels (a) and (d), where $\lambda = r_{avg}/R = 0.99$ and $\lambda = r_{avg}/R = 0.80$, respectively. Panel (b) illustrates the absolute amplitudes of the spherical harmonic functions $\hat{r}_l^m$ contained in the deformation pattern of panel (a). The analytical prediction for the number of dimples around the equator is $l_{cr} = 20$, corresponding to the observation that the majority of spherical harmonics constituting the solution fall within a narrow band around degree $l \sim 20$. Panel (c) displays the amplitudes of spherical harmonics for the stress function $\hat{\phi}_l^m$, which are concentrated at lower degrees l. Panel (e) shows the distribution of the spherical harmonic amplitudes $\hat{r}_l^m$ for the deformation pattern in panel (d). This distribution is significantly wider, whereas the $\hat{\phi}_l^m$ distribution in panel (f) remains similar to that in panel (c). In both simulations $R = 50$ mm, $h = 0.25$ mm, $E_f = 4$ MPa, $E_s = 0.9$ kPa and $\nu = \nu_s = 0.49$.

Compared to the classical numerical methods, such as the finite element method, which often face computational constraints when dealing with systems exhibiting numerous dimples due to the high number of degrees of freedom, our method offers a substantial reduction in computational load. This efficiency is achieved because only specific $\hat{r}_l^m$ amplitudes near l_{cr} are required for the calculations, owing to the banded nature of the solution.

Second, we investigate the impact of truncating the coefficients on the solution in the physical space. To do this, we solve a case where the coefficients $\hat{r}_l^m$ are concentrated around $l_{cr} = 20$, and the system is computed using spherical harmonic functions with degrees restricted to $l \leq l_{max} = 50$. We then calculate the physical representation by varying the number of included coefficients. Specifically, a triangular truncation is applied, limiting the coefficients $\hat{r}_l^m$ to $l_{max} = \{18, 20, 22, 24, \ldots, 50\}$, as depicted in Fig. 3 (a). Panel (b) illustrates the average normalized error, with the errors for a valley point and a ridge point shown in green, red, and blue, respectively. The points used for comparison are marked by red and blue crosses on the buckyballs in the figure.

It is important to note that, despite being presented in a log-linear plot, the average error (green curve) indicates that the most significant improvement in accuracy occurs up to $l_{max} \approx 24$. This can be attributed to the fact that the coefficients for degrees $16 \leq l_{max} \leq 24$ capture the majority of the pattern's essential information, while the higher-degree coefficients ($l_{max} > 24$) primarily account for finer details of the deformation pattern, such as the precise shape of the out-of-plane displacement surface.

It is important to emphasize also that, although the convergence tests were conducted using a nearly incompressible material with $\nu = \nu_s = 0.49$ to prevent volumetric locking of the substrate at $\nu_s = 0.5$, our method is not restricted to nearly incompressible materials. It can equally handle compressible materials while maintaining its convergence properties. As noted in the literature [26], these types of problems exhibit only a weak dependence on the Poisson's ratio. However, since here we are dealing with a sphere which becomes progressively stiffer for isometric deformations as $\nu_s \to 0.5$, it is important to check for a compressible cases. We include an analysis with a compressible substrate in Appendix, where we find no notable difference.
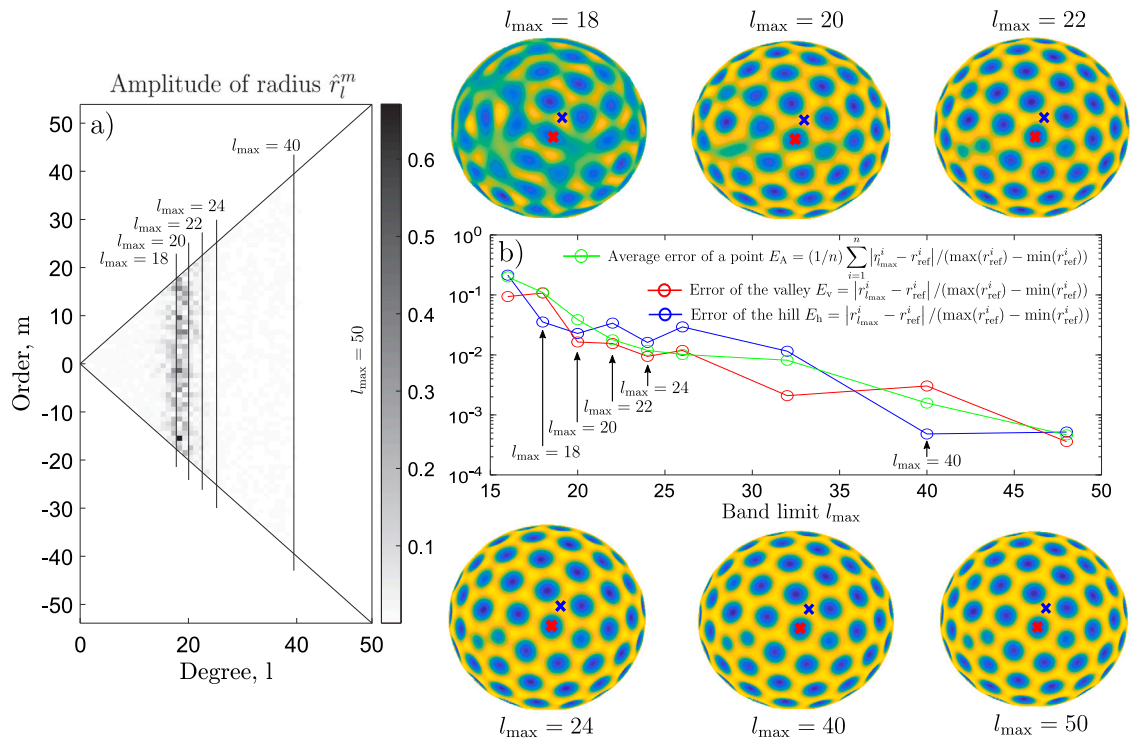
Fig. 3. Panel (a) shows the limits of the triangular truncation in the function space of the coefficients $\hat{r}_l^m$ for the case solved with coefficients of the maximum degree $l_{\max} = 50$. Panel (b) shows the average normalized error, the error in the valley and error in the ridge point with green, red and blue, respectively, for different truncation limits of the transformation from a function to the physical space. The valley and the ridge are also marked in the buckyballs with red and blue cross, respectively. In the simulation parameters $R = 50$ mm, $h = 0.25$ mm, $E_f = 4$ MPa, $E_s = 0.8$ kPa, $\nu = \nu_s = 0.49$ and $r_{\text{avg}}/R = 0.99$ were used.

4.2. Experimental validation of the method

We validate our numerical results with experiments shown in Fig. 4 that we made specifically for this task. In these experiments, the film was made from a polymer *QSil 550* and was fixed onto a substrate made from a softer polymer *Elite Double 8*. The substrate was further softened by the addition of a silicone oil (up to 50%). The load was induced by the shrinkage of the substrate during curing.

We measured the thickness of the film h, and performed compression tests to measure the Young's modulus of the film, which was $E_f = 5.2$ MPa and that of the substrate, which was either $E_s = 0.166$ MPa or $E_s = 0.065$ MPa depending on the amount of added silicone oil (25% and 50%, respectively). We also performed volumetric tests that confirmed the accuracy of the assumption of the (near) incompressibility with $\nu = 0.4995$ and $\nu_s = 0.4994$. Because these values are close to $\nu = 0.5$, which causes volumetric locking of the substrate, we assumed $\nu = \nu_s = 0.49$, which mitigates the locking phenomena, while at the same time does not affect the accuracy noticeably. Because the wavelength of the dimples/labyrinths (or equivalently the number of dimples/labyrinths along the equator) mainly depends on the thickness h of the substrate and ratio of the tangential moduli E_f/E_s, the wavelength L_{cr} can be calculated using Eq. (43) for a medium or large number of dimples even in the far post-critical regime.

On the other hand, the amount of shrinkage of the substrate, which governs the reduction in the average radius of the shell $r_{\text{avg}} = \lambda R$ and with that the magnitude of the wrinkles, is more difficult to measure. This would have been possible with an accurate and fast 3D scanning, which was not available. Fortunately, due to the near inextensibility of the thin films [3] the area of the surface before and after bifurcation stays approximately the same $\int_\Omega \left(\nabla\nabla r : \tilde{\nabla}\tilde{\nabla}r/2 + \Delta rr/R^2 + r^2/R^4 \right) d\Omega \approx 4\pi R^2$. This yields a geometric relation between the magnitudes of the wrinkles mainly described by $\int_\Omega \left(\nabla\nabla r : \tilde{\nabla}\tilde{\nabla}r/2 + \Delta rr/R^2 \right) d\Omega$ and the average radius of the shell, mainly described by $\int_\Omega r^2/R^4 d\Omega$. This can further be shown by rewriting the equation in terms of spherical harmonic function $\sum_{l=1}^{l_{\max}} \sum_{m=-l}^{l} (\nabla\nabla\hat{r})_l^m : (\tilde{\nabla}\tilde{\nabla}\hat{r})_l^m/2 - l(l+1)\hat{r}_l^m\hat{r}_l^m/R^2 + \hat{r}_l^m\hat{r}_l^m/R^4 + (\lambda^2 - 1)/R^2 = 0$. Because we know from Eqs. (31) and (32) that the operators $(\nabla\nabla\hat{r})_l^m$ and $(\tilde{\nabla}\tilde{\nabla}\hat{r})_l^m$ only depend on the wavelength l_{cr} and $-l_{\text{cr}} \le m \le l_{\text{cr}}$ there is a one-to-one connection between the shrinkage of the average radius $\lambda = r_{\text{avg}}/R$ and the magnitude of wrinkling patterns characterized by $\hat{r}_l^m$.

Our numerical results for the dimple patterns are given in panels (f)–(j) of Fig. 4. Because in the experiments the circular edge of the hemisphere on a certain latitude acts as a rather stiff rubber ring, which prevents any significant deformations, we use in our simulations an additional constraint on deformations on that latitude. We constrain the radial displacements $r(\theta = \theta_0, \varphi) = R$ and the gradient of the radial displacements $r_{,\theta}(\theta = \theta_0, \varphi) = 0$ in the direction of the polar angle. Since the constraints are given in
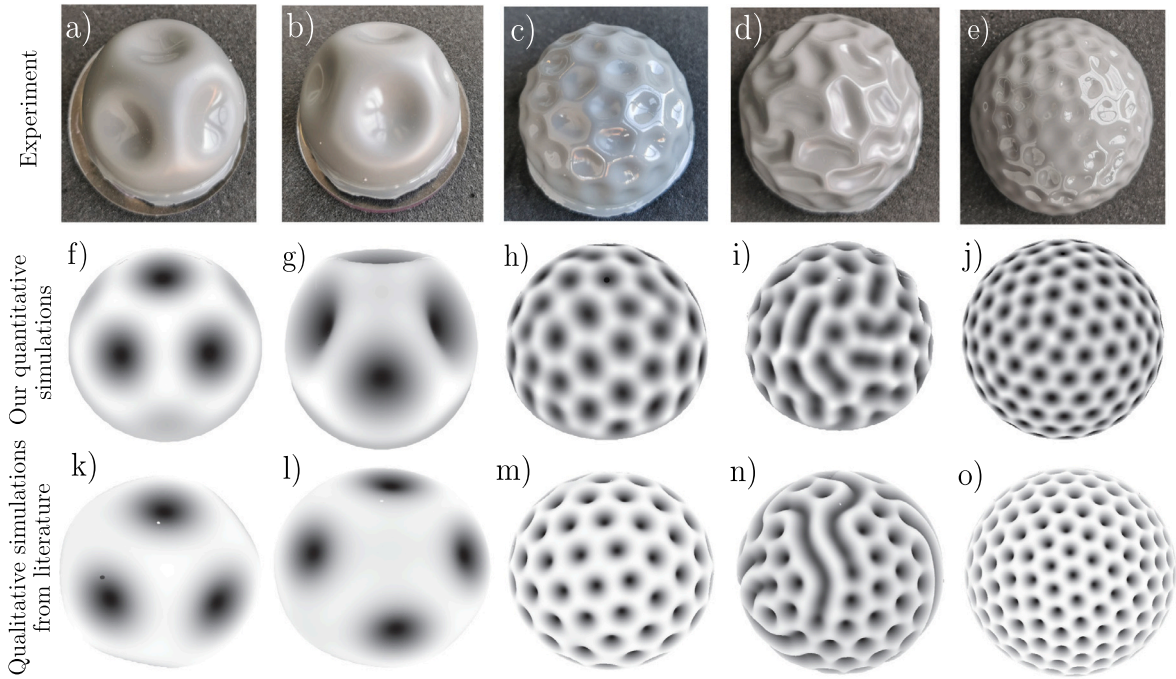
Fig. 4. Panels (a)–(e) show our experimentally obtained wrinkle patterns on a hemispherical film of thickness $h \in \{1.32, 1.32, 0.44, 0.44, 0.45\}$ mm and Young's modulus $E_f = 5.2$ MPa, fixed to a substrate with Young's modulus $E_s \in \{0.056, 0.056, 0.056, 0.056, 0.056, 0.166\}$ MPa. The depths of the wrinkles from top to bottom were $r_{max} - r_{min} \in \{7, 8, 1.6, 1.9, 0.6\}$ mm, and the initial radius of the hemispheres was $R = \{25, 25, 30, 30, 30\}$ mm. Panels (f)–(j) show the deformation patterns quantitatively predicted by our theory using the above material parameters. The predictions closely match the experimentally observed patterns. Panels (k)–(o) show the deformation patterns obtained by following the approach of [2] using our method.

the physical space in the integration points, we can write them as $r_i = R$ and $(r_{,\theta})_i = 0$. Additionally, they can be written in terms of the coefficients $\hat{r}_l^m$ as $r_i = M_{ij} \hat{r}_{l(j)}^{m(j)} = R$ and $(r_{,\theta})_i = K_{ij} \hat{r}_{l(j)}^{m(j)} = 0$, with K_{ij} being a spherical harmonics transformation matrix and $M_{ij} = H_{kj} K_{ik}$, where H_{ij} is the differentiation matrix with respect to θ. This way we have two additional linear constraints acting on the points of the latitude θ_0 to simulate the mentioned circular edge of the hemisphere in the experiments.

Additionally, panels (k)–(o) in Fig. 4 show the results of our simulations using the qualitative theory by [2], where a fit parameter is required to obtain the deformation pattern and as such offers only a qualitative prediction. Despite this limitation, it represents up until now the only rather robust computational method capable of reproducing the arrangement of dimples on the hemisphere as observed experimentally [1,11] and in their own experiments.

In comparing the results of our quantitative theory in panels (f)–(j) to and the results of the qualitative theory by [2] in panels (k)–(o) to our experimental results in panels (a)–(e), we notice that the dimples obtained from our theory are hexagonal and oval, as is the case in the experimental results. On the other hand, dimples from the qualitative theory [2] and the theories in [7,8] are slightly different, as they are more circular and the radial displacement is more concentrated in the center of the dimples. We hypothesize that this is due to the disregard of the membrane force equilibrium in these studies.

Our results in panels (f)–(j) show that the dimples and labyrinths resemble the shape and the distribution, which agree with the crystallographic rules on curved crystals [1,12]. This is possible because our method does not suffer from non-physical distribution of wrinkles because it is mesh free and because we consider tangential displacements in our theory. This is in stark contrast with the simulations made with other tools, such as in [7,15], where the deformation patterns are visibly influenced by the underlying numerical finite element mesh and the shape of the dimples and labyrinths is slightly different from the experimentally observed ones.

As can be seen from the results that our theory can describe the gradual elongation and coalescence of dimples that is also observed in the experiments as the load is increased, see e.g. panels (d) and j in Fig. 4.

4.3. Evolution of a deformation pattern with increasing load

Fig. 5 shows the development of a deformation pattern with increasing displacement controlled load.

Starting from an unloaded and undeformed shell with the initial radius R we continuously reduce the relative average radius $\lambda = r_{avg}/R$. Since we do not consider the energy of an isotropic compression of the spherical substrate, initially only the membrane
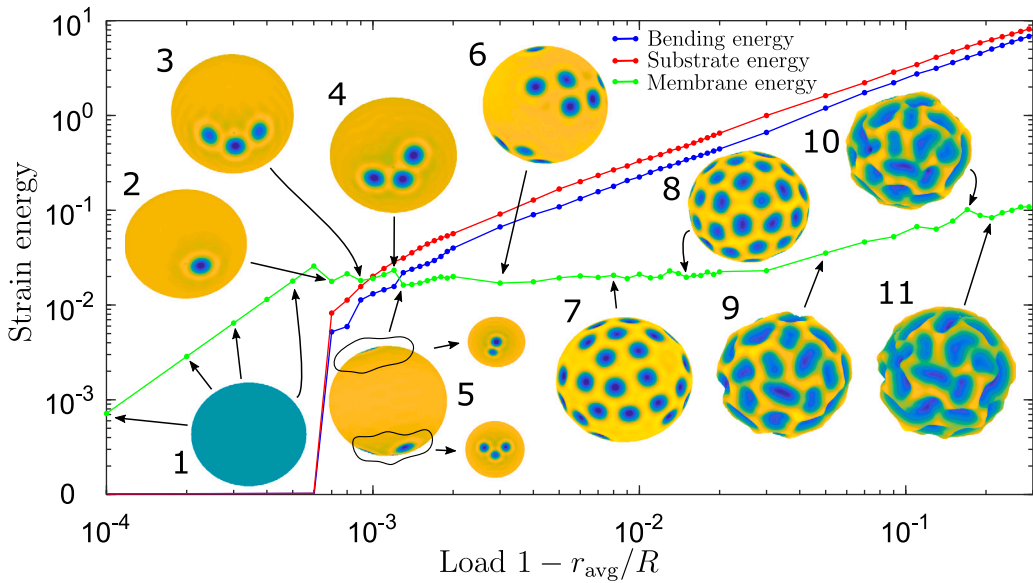
Fig. 5. Bending energy of the film, the membrane energy of the film and the strain energy of the substrate (excluding the energy of isotropic substrate compression) as a function of the increasing displacement load $1 - \lambda = 1 - r_{avg}/R$. The insets 1–11 show the corresponding deformation patterns. The parameters of the simulations were the same as given in the caption of Fig. 2, with the exception of the modulus of elasticity of the substrate, which was chosen to be such that it produces $l_{cr} = 15$ for good illustration.

energy increases (see the green curve and the inset 1). At the point where inset 2 is shown, it is energetically more favorable to bend the film instead of further isotropically deforming the film, thereby forming one dimple. In this way, some of the membrane energy is released at the expense of an increase in energy due to the bending of the film and the non-isotropic stretching of the substrate. In inset 3, additional dimples are formed to further release the membrane energy while slightly increasing the bending and substrate strain energy. The evolution of the pattern from the inset 3 to inset 4 shows that the rearrangement of the wrinkles represents another mechanism for releasing the membrane energy, as first shown experimentally in [1]. Inset 5 shows that wrinkles also form on the opposite side. Insets 6 and 7 show that the formation of additional wrinkles keeps the membrane energy approximately constant, while the bending and substrate strain energy increases approximately linearly with increasing displacement-controlled load. It can be seen in the inset 8 that due to the inability of the hexagonal lattice to cover the spherical surface due to topological constraints, the dimple lattice exhibits topological defects, which can be noticed from the fact that some dimples may have 5 or 7 adjacent dimples, while the majority have 6 dimples. When the load is further increased, inset 9 shows that after the entire surface has been populated with dimples and the release of membrane energy has become suppressed due to the formation of additional wrinkles, the dimples start to grow in one direction and become oval. In this way, the wrinkled area is further increased to a certain extent, but this way of releasing the membrane energy is not as efficient as it starts to grow slowly with the load. Insets 10 and 11 show additional widening of the oval dimples and the gradual transition to labyrinthine deformation patterns. Labyrinthine deformation patterns do not form in this particular system, even when the load is extremely increased. This will be examined in more detail in the next section.

4.4. Deformation patterns

In previous studies [1,6], it was demonstrated that the ratio between the radius of a sphere, denoted as R, and the wavelength of wrinkles, denoted as L_{cr}, plays a crucial role in determining the length-scale of wrinkling in compressed films on spherical substrates. Alternatively, the number of dimples along the equator, given by $l_{cr} = 2\pi R/L_{cr}$, serves as a measure of this length-scale and influences the overall system size. Notably, a system with a small number of wrinkles allows for fewer possible arrangements of dimples, making it relatively easier to solve compared to a larger system with numerous wrinkles.

The number of dimples along the equator can be relatively accurately determined using Eq. (43), which is based on the calculation of the dimple wavelength while neglecting the initial curvature. However, an important study by [15] demonstrated that considering the initial curvature, only one parameter governs the size of the system. This parameter, in conjunction with the influence of film bending and substrate effects, also accounts for membrane effects due to curvature. Unfortunately, an analytic expression for the wavelength of the dimples is not available.

Fortunately, the ratio of the tangential elastic moduli, the thickness of the film, and the initial curvature of the system — factors that determine the size of the system through the number of wrinkles — does not change significantly with the degree of deformation in wrinkling. Therefore, the expression from Eq. (43) or equivalently, the parameter from [15], remains valid long into the post-bifurcation regime.
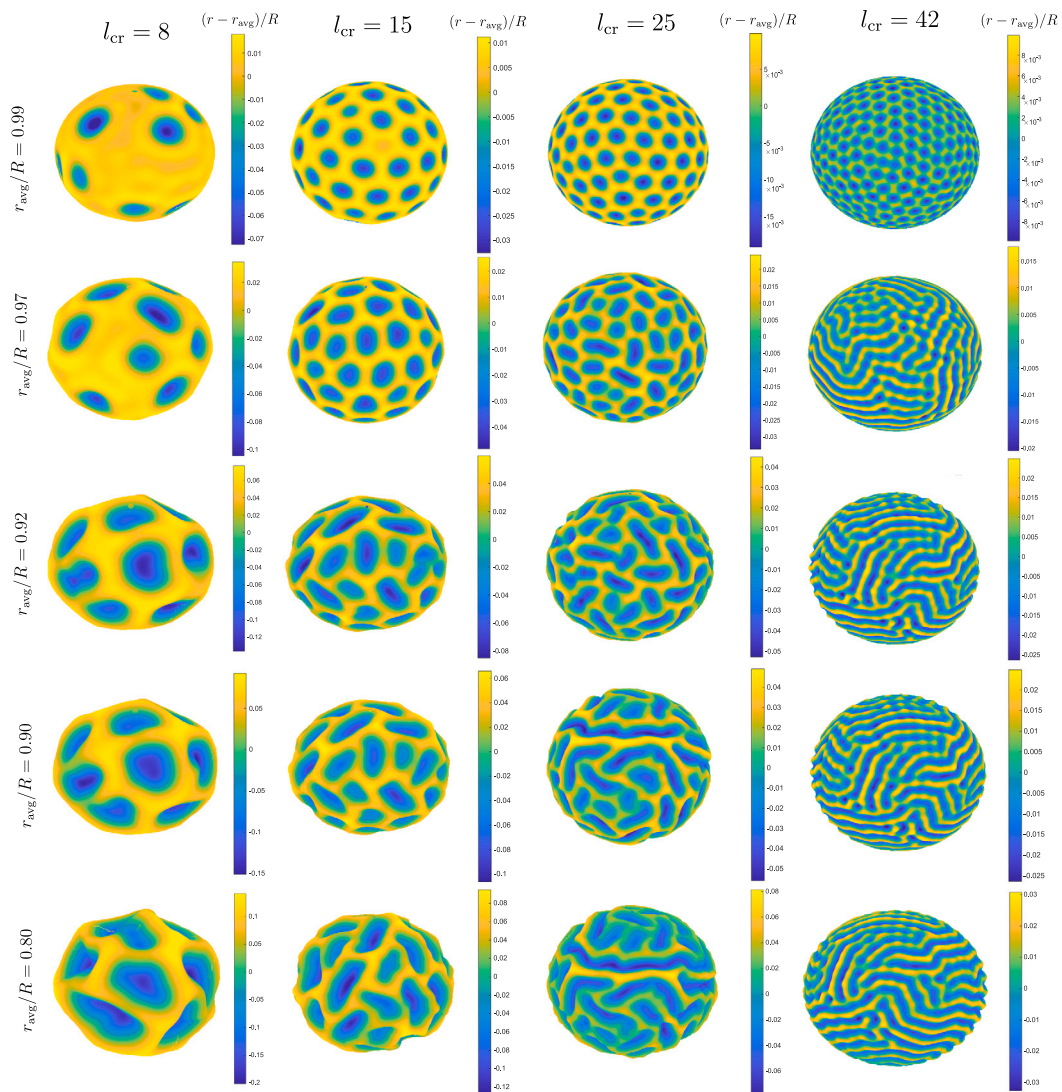
Fig. 6. Deformation patterns for different numbers of wrinkles l_{cr} and loads $\lambda = r_{avg}/R$. In the simulations the initial radius of the shells was $R = 50$ mm, the thickness of the film was $h = 0.25$ mm, the Young's modulus of the film was $E_f = 4$ MPa and the Poisson's ratios were $\nu = \nu_s = 0.49$.

However, these parameters do not characterize whether dimple, labyrinth, or bi-stable deformation patterns will occur. In Fig. 6, we illustrate different deformation patterns for various numbers of dimples along the equator ($l_{cr} = \{8, 15, 25, 42\}$) and loads ($\lambda = \{0.99, 0.97, 0.92, 0.90, 0.80\}$), while other material and geometric parameters are provided in the figure caption.

Fig. 6 illustrates that in the case with a small number of wrinkles, specifically with $l_{cr} = 8$ and $l_{cr} = 15$, dimples gradually emerge until they cover the entire surface. Subsequently, these dimples elongate in a single direction but fail to coalesce into a labyrinthine deformation pattern, and the reasons for this remains unexplained. Our hypothesis is that in small systems, e.g., $l_{cr} = 8$–25, under small loads, e.g., $r_{avg}/R = 0.99$–0.92, the initial curvature prevents the formation of labyrinth patterns. This is in contrast with wrinkling in planar films that have no initial curvature in which labyrinth patterns emerge instantly post bifurcation [26,52]. As the load increases r_{avg}/R, the dimples elongate, indicating a tendency toward longer labyrinth-like patterns. However, in small systems, e.g., $l_{cr} = 8$–15, under low load, e.g., $r_{avg}/R = 0.90$–0.80, something still inhibits the merging of elongated dimples into longer valleys. We assume that the emergent curvature plays a role in preventing this merging process.

In contrast, medium-sized systems, e.g., $l_{cr} = 25$, experiencing smaller loads, e.g., $r_{avg}/R = 0.99$–0.92, encounter an initial curvature that prevents the formation of labyrinth patterns. However, as the load increases, e.g., $r_{avg}/R = 0.90$–0.80, a mechanism favoring labyrinth-like deformation patterns emerges, surpassing the influence of the initial and emerging curvature.

In larger systems, e.g., with $l_{cr} = 42$, the lower initial curvature $1/R$ has a diminished effect, leading to a rapid evolution from the initial dimple configuration to the eventual labyrinth deformation pattern as the load increases.

5. Conclusion

In this paper we present a new version of a (less) reduced shell theory based on the Kirchhoff–Love shell theory. In contrast to other reduced theories that neglect tangential displacements and membrane equilibrium, our approach takes into account the linear effects of tangential displacements on the equilibrium of membrane forces, leading to the release of membrane stresses. Accurate modeling of membrane stresses is crucial, especially for problems where they dominate over bending stresses, such as wrinkling. Compared to other reduced Kirchhoff–Love shell theories, our approach leads to physically more meaningful results that are even quantitatively comparable to our own experimental results and those of other researchers.

In order to eliminate numerically induced imperfections, such as those arising from the presence of a (discrete) mesh, which can significantly affect the obtained deformation patterns, we develop a Galerkin-type pseudo-spectral method for representing functions on a spherical surface using spherical harmonic functions. With this approach, we can solve our shell model (and other shell models) on a sphere without having to use special finite elements, which can be cumbersome and are affected by spatial discretization effects.

Our solution concept is based on the minimization of the total potential energy under consideration the constraints. This robust approach effectively addresses our strongly non-convex optimization problem, where the deformation patterns are mainly governed by the geometric nonlinearities of the membrane stresses. Other solution methods found in the literature have significant problems dealing with this complexity. However, the constrained optimization framework automatically incorporates convexification as the constraints only gradually tighten during the iterative process.

Due to the combined difficulty of the need for dense meshes and extreme non-convexity of the energy landscape, modern numerical tools tailored for solving wrinkling problems were either too computationally costly, or relied on oversimplifications, making them unsuitable for analyzing the evolution of wrinkling in compressed films on curved substrates. The method presented in this paper enables efficient computation of deformation patterns that quantitatively match experimental results. It facilitates the investigation of the mechanisms responsible for the formation of dimples and their transition into labyrinth patterns. Nevertheless, the method could be further improved by a more accurate nonlinear model of the substrate (e.g. a neo-Hookean material model), which would also increase the numerical stability. Additionally, it is worth mentioning that although the stress function approach is also possible in case a nonlinear substrate model is employed, a displacement formulation is probably less convoluted and therefore more useful, even though it introduces additional degrees of freedom.

CRediT authorship contribution statement

Jan Zavodnik: Writing – original draft, Visualization, Software, Methodology, Investigation, Formal analysis, Data curation, Conceptualization. **Miha Brojan:** Writing – review & editing, Supervision, Resources, Methodology, Investigation, Funding acquisition, Conceptualization.

Declaration of competing interest

The authors declare that they have no known competing financial interests or personal relationships that could have appeared to influence the work reported in this paper.

Acknowledgment

Appendix. Convergence of the method with a compressible substrate

In Fig. A.1 we demonstrate that the method is appropriate for both, the incompressible and compressible materials. Panel (a) shows the results of a simulation using the parameters $R = 50$ mm, $h = 0.25$ mm, $E_f = 4$ MPa, $E_s = 0.8$ kPa and $\nu = \nu_s = 0.49$, while panel (b) shows a simulation with the same parameters, except that $\nu = \nu_s = 0.3$. The deformation patterns are qualitatively similar and differ only due to the solver finding a different stable equilibrium state.

Data availability

Data will be made available on request.

a) Nearly incompressible material $\nu = \nu_s = 0.49$ b) Compressible material $\nu = \nu_s = 0.30$
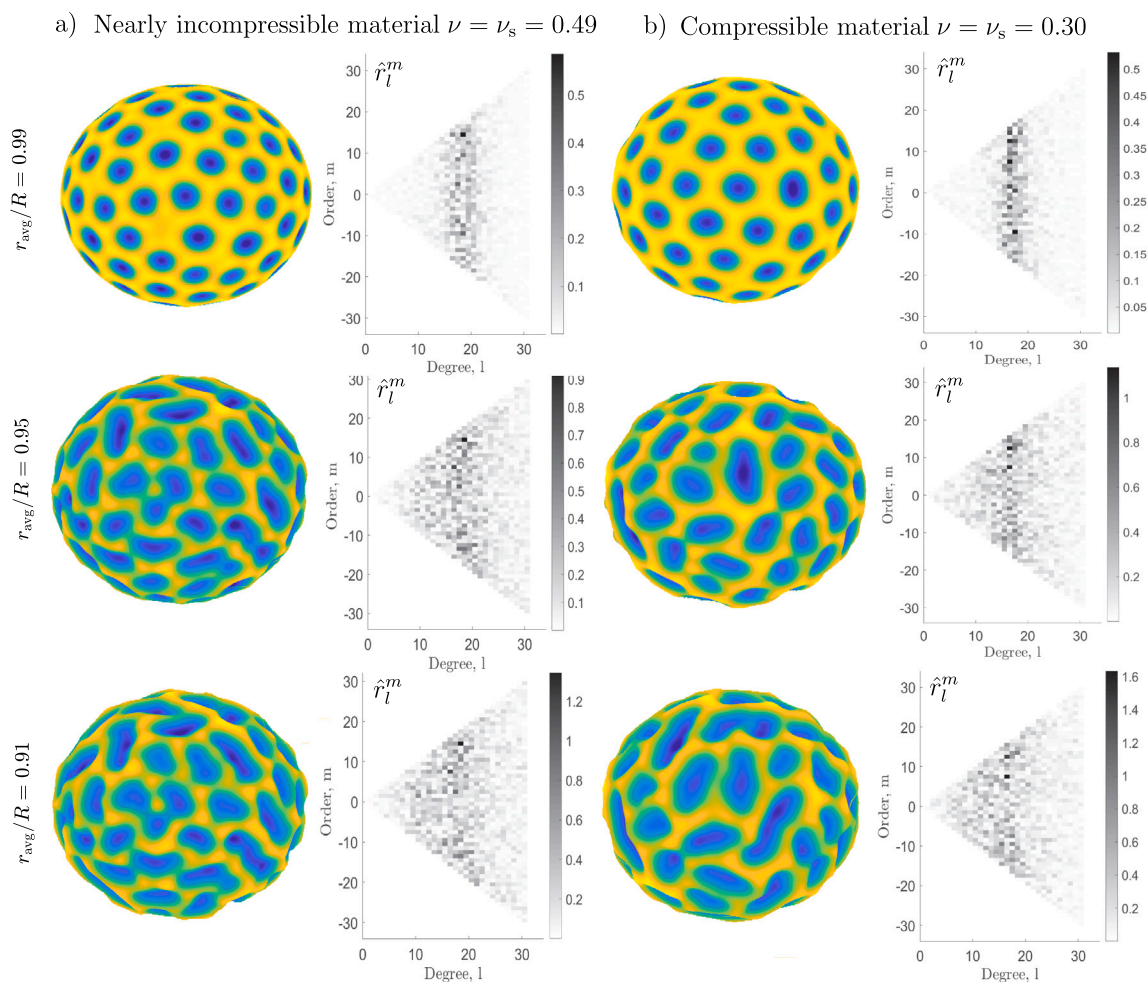

Fig. A.1. The rows contain results in the physical and functional space for a nearly incompressible material in row (a) and a compressible material in row (b). In all three lines where the load changes there are no noticeable differences between the results, except that the wavelength of the deformation pattern in a nearly incompressible case is a bit smaller.

References

[1] M. Brojan, D. Terwagne, R. Lagrange, P.M. Reis, Wrinkling crystallography on spherical surfaces, Proc. Natl. Acad. Sci. 112 (1) (2015) 14–19, http://dx.doi.org/10.1073/pnas.1411559112, arXiv:https://www.pnas.org/doi/pdf/10.1073/pnas.1411559112, URL https://www.pnas.org/doi/abs/10.1073/pnas.1411559112.

[2] N. Stoop, R. Lagrange, D. Terwagne, P.M. Reis, J. Dunkel, Curvature-induced symmetry breaking determines elastic surface patterns, Nature Mater. 14 (3) (2015) 337–342, http://dx.doi.org/10.1038/nmat4202.

[3] J. Zavodnik, M. Brojan, Effects of nonlinearities and geometric imperfections on multistability and deformation localization in wrinkling films on planar substrates, J. Mech. Phys. Solids 191 (2024) 105774, http://dx.doi.org/10.1016/j.jmps.2024.105774, URL https://www.sciencedirect.com/science/article/pii/S0022509624002400.

[4] J. Zavodnik, A. Košmrlj, M. Brojan, Rate-dependent evolution of wrinkling films due to growth on semi-infinite planar viscoelastic substrates, J. Mech. Phys. Solids 173 (2023) 105219, http://dx.doi.org/10.1016/j.jmps.2023.105219, URL https://www.sciencedirect.com/science/article/pii/S0022509623000236.

[5] D.A. Matoz-Fernandez, F.A. Davidson, N.R. Stanley-Wall, R. Sknepnek, Wrinkle patterns in active viscoelastic thin sheets, Phys. Rev. Res. 2 (2020) 013165, http://dx.doi.org/10.1103/PhysRevResearch.2.013165, URL https://link.aps.org/doi/10.1103/PhysRevResearch.2.013165.

[6] S. Cai, D. Breid, A. Crosby, Z. Suo, J. Hutchinson, Periodic patterns and energy states of buckled films on compliant substrates, J. Mech. Phys. Solids 59 (5) (2011) 1094–1114, http://dx.doi.org/10.1016/j.jmps.2011.02.001, URL https://www.sciencedirect.com/science/article/pii/S0022509611000299.

[7] T. Veldin, B. Brank, M. Brojan, Computational finite element model for surface wrinkling of shells on soft substrates, Commun. Nonlinear Sci. Numer. Simul. 78 (2019) 104863, http://dx.doi.org/10.1016/j.cnsns.2019.104863, URL https://www.sciencedirect.com/science/article/pii/S1007570419301832.

[8] T. Veldin, M. Lavrenčič, B. Brank, M. Brojan, A comparison of computational models for wrinkling of pressurized shell-core systems, Int. J. Non-Linear Mech. 127 (2020) 103611, http://dx.doi.org/10.1016/j.ijnonlinmec.2020.103611, URL https://www.sciencedirect.com/science/article/pii/S0020746220302730.

[9] T. Veldin, B. Brank, M. Brojan, Discrete Kirchhoff–Love shell quadrilateral finite element designed from cubic Hermite edge curves and Coons surface patch, Thin-Walled Struct. 168 (2021) 108268, http://dx.doi.org/10.1016/j.tws.2021.108268, URL https://www.sciencedirect.com/science/article/pii/S0263823121004894.

[10] V. Vitelli, J.B. Lucks, D.R. Nelson, Crystallography on curved surfaces, Proc. Natl. Acad. Sci. 103 (33) (2006) 12323–12328, http://dx.doi.org/10.1073/pnas.0602755103, arXiv:https://www.pnas.org/doi/pdf/10.1073/pnas.0602755103, URL https://www.pnas.org/doi/abs/10.1073/pnas.0602755103.

[11] D. Breid, A.J. Crosby, Curvature-controlled wrinkle morphologies, Soft Matter 9 (2013) 3624–3630, http://dx.doi.org/10.1039/C3SM27331H.

[12] F. Jiménez-López, N. Stoop, R. Lagrange, J. Dunkel, P.M. Reis, Curvature-controlled defect localization in elastic surface crystals, Phys. Rev. Lett. 116 (2016) 104301, http://dx.doi.org/10.1103/PhysRevLett.116.104301, URL https://link.aps.org/doi/10.1103/PhysRevLett.116.104301.

[13] T. Erber, G.M. Hockney, Equilibrium configurations of N equal charges on a sphere, J. Phys. A: Math. Gen. 24 (23) (1991) L1369, http://dx.doi.org/10.1088/0305-4470/24/23/008.

[14] M.J. Bowick, L. Giomi, Two-dimensional matter: order, curvature and defects, Adv. Phys. 58 (5) (2009) 449–563, http://dx.doi.org/10.1080/00018730903043166.

[15] F. Xu, S. Zhao, C. Lu, M. Potier-Ferry, Pattern selection in core-shell spheres, J. Mech. Phys. Solids 137 (2020) 103892, http://dx.doi.org/10.1016/j.jmps.2020.103892, URL https://www.sciencedirect.com/science/article/pii/S0022509619310567.

[16] Y. Wang, Y. Du, F. Xu, Strain stiffening retards growth instability in residually stressed biological tissues, J. Mech. Phys. Solids 178 (2023) 105360, http://dx.doi.org/10.1016/j.jmps.2023.105360, URL https://www.sciencedirect.com/science/article/pii/S0022509623001643.

[17] B. Li, F. Jia, Y.-P. Cao, X.-Q. Feng, H. Gao, Surface wrinkling patterns on a core-shell soft sphere, Phys. Rev. Lett. 106 (2011) 234301, http://dx.doi.org/10.1103/PhysRevLett.106.234301, URL https://link.aps.org/doi/10.1103/PhysRevLett.106.234301.

[18] M. Lavrenčič, B. Brank, M. Brojan, Multiple wrinkling mode transitions in axially compressed cylindrical shell-substrate in dynamics, Thin-Walled Struct. 150 (2020) 106700, http://dx.doi.org/10.1016/j.tws.2020.106700, URL https://www.sciencedirect.com/science/article/pii/S0263823119319391.

[19] T. Wang, Z. Dai, M. Potier-Ferry, F. Xu, Curvature-regulated multiphase patterns in Tori, Phys. Rev. Lett. 130 (2023) 048201, http://dx.doi.org/10.1103/PhysRevLett.130.048201, URL https://link.aps.org/doi/10.1103/PhysRevLett.130.048201.

[20] F. Cirak, M. Ortiz, P. Schröder, Subdivision surfaces: a new paradigm for thin-shell finite-element analysis, Internat. J. Numer. Methods Engrg. 47 (12) (2000) 2039–2072, http://dx.doi.org/10.1002/(SICI)1097-0207(20000430)47:12<2039::AID-NME872>3.0.CO;2-1.

[21] C. Canuto, A. Quarteroni, Spectral methods, in: Encyclopedia of Computational Mechanics Second Edition, John Wiley & Sons, Ltd, 2017, pp. 1–16, http://dx.doi.org/10.1002/9781119176817.ecm2003m.

[22] N.L. Trefethen, Front matter, in: Spectral Methods in MATLAB, SIAM, 2000, pp. i–xvii, http://dx.doi.org/10.1137/1.9780898719598.fm, URL https://epubs.siam.org/doi/abs/10.1137/1.9780898719598.fm.

[23] Y. Lecieux, R. Bouzidi, Numerical wrinkling prediction of thin hyperelastic structures by direct energy minimization, Adv. Eng. Softw. 50 (2012) 57–68, http://dx.doi.org/10.1016/j.advengsoft.2012.02.010, CIVIL-COMP, URL https://www.sciencedirect.com/science/article/pii/S0965997812000415.

[24] S. Sriram, E. Polukhov, M.-A. Keip, Transient stability analysis of composite hydrogel structures based on a minimization-type variational formulation, Int. J. Solids Struct. 230–231 (2021) 111080, http://dx.doi.org/10.1016/j.ijsolstr.2021.111080, URL https://www.sciencedirect.com/science/article/pii/S0020768321001700.

[25] J. Simo, D. Fox, On a stress resultant geometrically exact shell model. Part I: Formulation and optimal parametrization, Comput. Methods Appl. Mech. Engrg. 72 (3) (1989) 267–304, http://dx.doi.org/10.1016/0045-7825(89)90002-9, URL https://www.sciencedirect.com/science/article/pii/0045782589900029.

[26] B. Audoly, A. Boudaoud, Buckling of a stiff film bound to a compliant substrate—Part I:: Formulation, linear stability of cylindrical patterns, secondary bifurcations, J. Mech. Phys. Solids 56 (7) (2008) 2401–2421, http://dx.doi.org/10.1016/j.jmps.2008.03.003.

[27] Z. Huang, W. Hong, Z. Suo, Nonlinear analyses of wrinkles in a film bonded to a compliant substrate, J. Mech. Phys. Solids 53 (9) (2005) 2101–2118, http://dx.doi.org/10.1016/j.jmps.2005.03.007, URL https://www.sciencedirect.com/science/article/pii/S0022509605000700.

[28] B. Schutz, A First Course in General Relativity, second ed., Cambridge University Press, 2009.

[29] M.H. Sadd, Elasticity: Theory, Applications, and Numerics, Elsevier Butterworth Heinemann, 2005, XII, 461.

[30] M. do Carmo, Riemannian Geometry, in: Mathematics (Boston, Mass.), Birkhäuser, 1992, URL https://books.google.it/books?id=uXJQQgAACAAJ.

[31] S.S. Chern, W.H. Chen, K.S. Lam, Lectures on Differential Geometry, WORLD SCIENTIFIC, 1999, http://dx.doi.org/10.1142/3812.

[32] V.I. Kushch, Chapter 4 - Elastic solids with spherical inclusions, in: V.I. Kushch (Ed.), Micromechanics of Composites, Butterworth-Heinemann, Boston, 2013, pp. 69–117, http://dx.doi.org/10.1016/B978-0-12-407683-9.00004-7, URL https://www.sciencedirect.com/science/article/pii/B9780124076839000047.

[33] J.P. Boyd, Chebyshev and Fourier Spectral Methods, second ed., in: Dover Books on Mathematics, Dover Publications, Mineola, NY, 2001.

[34] F. Sansò, Erratum to: On the aliasing problem in the spherical harmonic analysis, Bull. Geod. 64 (1990) 313–330, http://dx.doi.org/10.1007/BF02538406.

[35] J.C. Adams, P.N. Swarztrauber, SPHEREPACK 3.0: A model development facility, Mon. Weather Rev. 127 (8) (1999) 1872–1878, http://dx.doi.org/10.1175/1520-0493(1999)127<1872:SAMDF>2.0.CO;2, URL https://journals.ametsoc.org/view/journals/mwre/127/8/1520-0493_1999_127_1872_samdf_2.0.co_2.xml.

[36] The MathWorks Inc, MATLAB Version: 9.11.0.1873467 (R2021b) Update 3, The MathWorks Inc., Natick, Massachusetts, United States, 2022, URL https://www.mathworks.com.

[37] A. Edmonds, Angular Momentum in Quantum Mechanics, in: Investigations in Physics Series, Princeton University Press, 1996, URL https://books.google.si/books?id=0BSOg0oHhZ0C.

[38] E. Butkov, Mathematical Physics, Addison-Wesley Publ., Reading, Mass, 1973, URL https://www.worldcat.org/title/mathematical-physics/oclc/1067927488&referer=brief_results.

[39] A. Forte, W. Peltier, The kinematics and dynamics of poloidal-toroidal coupling in mantle flow: The importance of surface plates and lateral viscosity variations, Adv. Geophys. 36 (1994) 1–119, http://dx.doi.org/10.1016/S0065-2687(08)60537-3.

[40] M. Mohlenkamp, A user's guide to spherical harmonics, 2000.

[41] O. Colombo, Numerical methods for harmonic analysis on the sphere, 1981, p. 149.

[42] G. Wysin, Associated Legendre functions and dipole transition matrix elements, 2011, online lecture notes.

[43] P.N. Swarztrauber, The vector harmonic transform method for solving partial differential equations in spherical geometry, Mon. Weather Rev. 121 (12) (1993) 3415–3437, http://dx.doi.org/10.1175/1520-0493(1993)121<3415:TVHTMF>2.0.CO;2, URL https://journals.ametsoc.org/view/journals/mwre/121/12/1520-0493_1993_121_3415_tvhtmf_2_0_co_2.xml.

[44] Recurrence relations for Spherical harmonic functions: http://functions.wolfram.com/05.10.20.0001.01, 18.5.2024, 2011.

[45] J. Keiner, S. Kunis, D. Potts, Using NFFT 3—A software library for various nonequispaced fast Fourier transforms, ACM Trans. Math. Software 36 (2009) http://dx.doi.org/10.1145/1555386.1555388.

[46] U. Elahi, Sampling and Reconstruction of Spherical Signals for Applications in Cosmology, Acoustics and Beyond (Ph.D. thesis), College Engineering and Computer Science, College of Engineering and Computer Science, The Australian National University, 2019.

[47] A. Wächter, L.T. Biegler, On the implementation of an interior-point filter line-search algorithm for large-scale nonlinear programming, Math. Program. 106 (1) (2006) 25–57, http://dx.doi.org/10.1007/s10107-004-0559-y.

[48] N.-Y. Chiang, V.M. Zavala, An inertia-free filter line-search algorithm for large-scale nonlinear programming, Comput. Optim. Appl. 64 (2) (2016) 327–354, http://dx.doi.org/10.1007/s10589-015-9820-y.

[49] G.P. McCormick, Computability of global solutions to factorable nonconvex programs: Part I — Convex underestimating problems, Math. Program. 10 (1) (1976) 147–175, http://dx.doi.org/10.1007/BF01580665.

[50] H. Tuy, N. Van Thuong, On the global minimization of a convex function under general nonconvex constraints, Appl. Math. Optim. 18 (1) (1988) 119–142, http://dx.doi.org/10.1007/BF01443618.

[51] M. Tawarmalani, N.V. Sahinidis, Convexification and Global Optimization in Continuous And Mixed-Integer Nonlinear Programming, Kluwer Academic Publishers, USA, 2002.

[52] X. Chen, J.W. Hutchinson, Herringbone buckling patterns of compressed thin films on compliant substrates, J. Appl. Mech. 71 (5) (2004) 597–603, http://dx.doi.org/10.1115/1.1756141, arXiv:https://asmedigitalcollection.asme.org/appliedmechanics/article-pdf/71/5/597/5471575/597_1.pdf.